

Electromagnetically Induced Transparency

A Thesis
Presented to
The Division of Mathematics and Natural Sciences
Reed College

In Partial Fulfillment
of the Requirements for the Degree
Bachelor of Arts

Wesley W. Erickson

May 2012

Approved for the Division
(Physics)

Lucas Illing

Acknowledgements

There are many people that have made this year and this thesis an excellent culmination to my career at Reed. While I cannot list them all here, I especially wish to thank

- Lucas Illing, my advisor, whose encouragement and pointed guidance have made this thesis an absolutely enjoyable experience;
- my parents, who have given enthusiastic support and fended off the brunt of the world while I have been here;
- Bob Ormond, who constructed half of the electronics used in this thesis, helped me build more, and has a brilliant collection of stories;
- Greg Eibel, who has always been available for the miscellaneous milling and drilling, as well as a good conversation;
- Jay Ewing, who generously allowed me the use of more lab equipment than is probably reasonable;
- Nate, Antonio, and Neal, some of the first people I met at Reed who I have shared much with over these past four years - take physics and win it!
- Lindsay and Julia, who lived in the physics labs, were happy to listen to my tirades, ask pertinent questions, and always radiate vivacity;
- Angelynn and Anika, who revitalized me this past semester;
- and lastly Mad Science, in all its forms.

Thank you!

Table of Contents

Introduction	1
Chapter 1: Derivation	5
1.1 Outline	5
1.2 Deriving the EIT Hamiltonian	7
1.3 Rotating Wave Approximation	9
1.4 Corotating Frame	11
1.5 Density Operators	13
1.6 The Von Neumann Equation	14
1.7 Solving for the Density Matrix Elements	16
1.8 From Density to Susceptibility	18
1.9 Qualitative Predictions	20
Chapter 2: Experimental Setup	25
2.1 Atomic Structure of Rubidium	25
2.2 Optical Setup for EIT	26
2.2.1 Diode Laser	26
2.2.2 Saturated Absorption Spectroscopy	27
2.2.3 Primary Optical Setup	29
2.3 Electronics	31
2.4 Electro-Optic Modulator	32
2.5 Data Collection	36
Chapter 3: Results and Discussion	39
3.1 Collected Data	39
3.1.1 Corrections	39
3.1.2 Analysis	41
3.2 Improvements	43
3.2.1 Reducing Decoherence	43
3.2.2 EOM Drift	44
3.2.3 Real Time Scanning	44
Conclusion	47
References	49

List of Figures

1	Simple EIT Plot.	2
2	Energy levels of a 3-level Λ atom.	2
1.1	EIT capable systems.	6
1.2	Lambda atom with detunings and decay.	6
1.3	Electric susceptibility demonstrating EIT	20
1.4	EIT and control laser power	21
1.5	EIT and increasing decoherence.	21
1.6	EIT Doppler broadened for selected velocities.	23
1.7	EIT Doppler broadened with numerical integration.	23
2.1	^{87}Rb D2 lines.	26
2.2	Diagram of Doppler-free saturated absorption spectroscopy.	28
2.3	Doppler free saturated absorption spectroscopy trace.	28
2.4	Schematic of optical setup.	30
2.5	Instrument block diagram.	31
2.6	Schematic of an electro-optic modulator.	32
2.7	Gain curve of an amplitude EOM.	33
2.8	EOM viewed on Fabry-Perot interferometer, DC adjustment.	35
2.9	EOM viewed on Fabry-Perot interferometer, large V_{RF}	36
2.10	Laser Power vs. Current.	37
3.1	Experimental EIT absorption spectra.	40
3.2	Spatial dependence of absorption contributions.	42
3.3	Pumping effects.	43

Abstract

This thesis investigates electromagnetically induced transparency (EIT) in thermal rubidium vapor. EIT is a phenomenon that dramatically modifies the optical properties of a medium by creating a transparency window at a normally highly absorbing atomic resonance, and by greatly enhancing the medium's dispersion. The electric susceptibility describing these properties is derived, and an experimental setup to observe the effect is detailed, including results demonstrating EIT in Rubidium 87.

Introduction

This thesis explores electromagnetically induced transparency (EIT), a technique capable of drastically modifying a medium's optical properties near an atomic resonance when an electromagnetic field is applied. As the name indicates, these properties include a transparency window at a normally highly absorbing resonance, but in addition to this, the dispersion properties of the medium are greatly enhanced. The observed effect is shown in Fig. 1. EIT allows for many new phenomenon, including efficient non-linear mixing, slow light, and lasing without inversion to name a few.

EIT was first predicted in 1989 in a theoretical work employing aspects of coherent population trapping by Harris et al. [1]. An experimental realization of the effect was demonstrated shortly thereafter by Boller et al. [2] in Strontium vapor, and by Field et al. [3] in lead vapor. Ever since the first few papers on EIT were published by Harris et al., the number of papers mentioning the term have exponentially increased, and a wide range of phenomenon have been investigated that employ EIT: Highly efficient nonlinear mixing was confirmed by Jain et al. [4], where an intense 425 nm beam was converted to a 293 nm beam with 40% efficiency. Group velocities as slow as 8 m/s were induced by Budker et al. [5], a reduction by a factor of 10^7 from the speed of light in vacuum. A gaseous diffraction grating was proposed and confirmed by Ling et al. [6]. These are just a few of many novel applications; for many more see the review articles by Fleischhauer et al. [7] and by Marangos [8].

EIT is achievable only in atoms with specific energy structures. For a three level system (see Fig. 2), EIT requires two dipole allowed transitions ($|1\rangle \rightarrow |3\rangle$ and $|2\rangle \rightarrow |3\rangle$) and one forbidden transition ($|1\rangle \rightarrow |2\rangle$ is dipole forbidden). A strong laser, what we term the control laser, is tuned to the resonant frequency of the upper two levels. Then, a weak probe laser is scanned in frequency across the other transition. The medium is observed to have the properties plotted in Fig. 1 in response to the probe beam.

So far, we have only mentioned the observed phenomenon, not the underlying mechanics - a somewhat heuristic explanation of the phenomenon is as follows: Quantum

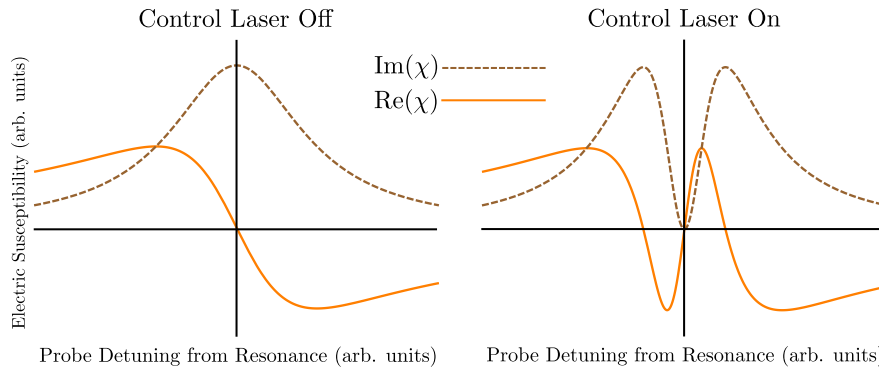


Figure 1: Simple EIT Plot. Here we are plotting the real and imaginary components of the complex linear susceptibility. The imaginary component corresponds to absorption - on the left we see a typical Lorentzian absorption peak while the control laser is inactive. When the control laser is applied, the absorption peak splits revealing a transparency at what was the maximal absorption. The real components appear in the dispersion relation, relating wave speed to frequency.

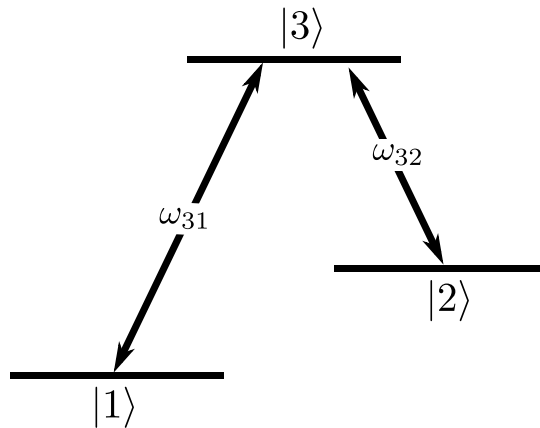


Figure 2: Energy levels of a 3-level Λ atom. The Λ atom has dipole allowed transitions $|1\rangle \rightarrow |3\rangle$ and $|2\rangle \rightarrow |3\rangle$. ω_{ij} is the resonant frequency for the transition.

mechanics requires that when multiple excitation pathways exist, interference between their probability amplitudes will occur [9]. This phenomenon is not unique to EIT and has been readily observed in many systems, for example quantum beats [10]. This leads to one possible picture of EIT as an interference between transition pathways. In the three level atom shown in Fig. 2, the atoms will primarily accumulate in the lowest energy state $|1\rangle$. Ordinarily, when one applies an electromagnetic field of frequency ω_{31} , atoms in the ground state can absorb energy and transition to state $|3\rangle$. But, when an electromagnetic field resonant with the $|2\rangle \rightarrow |3\rangle$ transition is also applied, there are now two transition pathways by which an atom can get from the ground state to the excited state: it can either transition in the same way as before, $|1\rangle \rightarrow |3\rangle$, or it can transition along $|1\rangle \rightarrow |3\rangle \rightarrow |2\rangle \rightarrow |3\rangle$. These two allowed transition paths can destructively interfere, and under the appropriate conditions this results in zero probe absorption at resonance.

The most interesting effect of EIT is not the transparency itself - this level of transparency could be achieved by tuning our laser away from the atomic resonance. What is particularly interesting is that EIT also induces large dispersion effects at the atomic resonance. In particular, a very steep linear dispersion relation is found at the point of minimal absorption. This steep dispersion relation is ultimately responsible for the fascinating phenomena of efficient mixing and slow group velocities mentioned earlier.

This thesis is primarily an experimental thesis. Chapter 1 gives a derivation of the transparency and dispersion results in a 3 level EIT system, and the qualitative predictions we expect to see in our experiment. The experimental setup for observing EIT in thermal rubidium vapor is explained in Chapter 2, and Chapter 3 shows our experimental results. Lastly, we conclude with some implications of EIT and possible extensions to this work.

Chapter 1

Derivation

To properly characterize EIT, we will employ a semiclassical approach. The atoms are treated as fully quantum objects, while all fields are treated as classical vector fields. There are fully quantum derivations of EIT [11], but we will not discuss them in this thesis, as the semiclassical treatment makes excellent predictions for atom-field interactions¹.

The derivation of EIT in this chapter primarily follows derivations shown in Weatherall [12] and Scully and Zubairy [13]. Additionally, much interpretation is drawn from Fleischhauer et al. [7].

1.1 Outline

There are three energy level configurations for three level atoms that can demonstrate EIT, shown in Fig. 1.1. While all three systems demonstrate EIT, we will be deriving EIT for a three level Λ -atom, as the effects are diminished in cascade and V systems due to high decay rates from $|2\rangle$, which shortens the coherence lifetime. The Λ -atom's $|2\rangle$ state is a metastable state with greatly reduced decays and longer coherence lifetimes.

We are ultimately interested in the optical properties of the medium, specifically the dispersion and absorption of the probe laser. These characteristics are described to first order by the frequency dependent complex valued linear electric susceptibility χ , which is defined by

$$\mathbf{P} = \epsilon_0 \chi \mathbf{E}, \tag{1.1}$$

¹A notable error of the semiclassical model is the lack of spontaneous emission - we account for this by adding phenomenological decay terms.

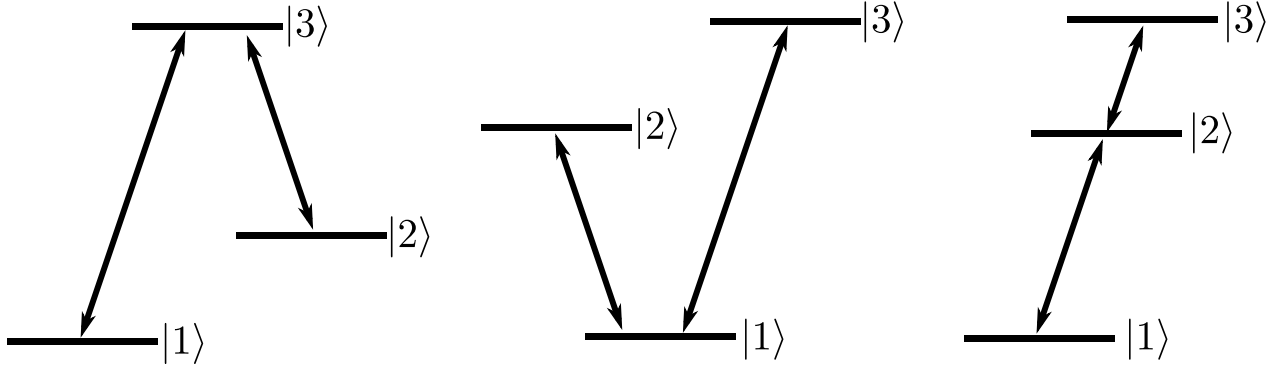


Figure 1.1: EIT capable systems. All three level systems capable of demonstrating EIT have one of three possible energy level structures: Λ type, V type, and cascade types. Each has two dipole allowed transitions and one dipole forbidden transition, with the only difference being the relative arrangement of the energy levels.

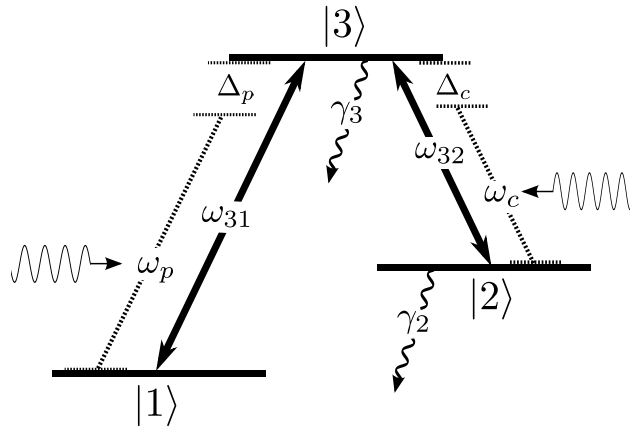


Figure 1.2: Lambda atom with detunings and decay. This figure shows the atomic system we will be working with throughout this thesis. States $|1\rangle \rightarrow |3\rangle$ are resonant with frequency $\omega_{31} = \omega_3 - \omega_1$, states $|2\rangle \rightarrow |3\rangle$ are resonant with frequency $\omega_{32} = \omega_3 - \omega_2$. These transitions are driven, respectively, with a probe laser of frequency ω_p and control laser of frequency ω_c . The probe laser is detuned from resonance by $\Delta_p = \omega_p - \omega_{31}$, while the control laser is detuned from resonance by $\Delta_c = \omega_c - \omega_{32}$. The upper states have a decay rate γ_3 and γ_2 , while the ground state is stable. The transition $|1\rangle \rightarrow |2\rangle$ is dipole forbidden, resulting in a very small γ_2 ($|2\rangle$ is a metastable state).

where \mathbf{P} is the dielectric polarization of the medium, \mathbf{E} is the electric field, and ϵ_0 is the permittivity of free space. Knowledge of χ completely determines the material properties we are seeking. Note that \mathbf{P} , \mathbf{E} and χ are all macroscopic quantities. However, in order to find χ , we need to consider individual atoms.

We first need a description of how the quantum mechanical atom behaves in the applied field. For this we construct a Hamiltonian (H_0) describing the three level atom, and approximate the field's effects as a dipole perturbation (H_1), which is given as the energy of the dipole moment operator ($\hat{\rho}$). The full Hamiltonian ($H = H_0 + H_1$) can be massaged with some approximations and transformations to a more agreeable form, what we term the EIT Hamiltonian (H_{EIT}).

The EIT Hamiltonian describes a single atom interacting with the external electromagnetic field, but in our system we have an ensemble of atoms. It is therefore natural to transition from describing the system with single atom wave functions, to describing it with density operators (ρ), which model the state of a population of atoms. From this description of the medium, we can generate an expression of the macroscopic polarization in terms of the expectation of the dipole moment operators ($\mathbf{P} = N\langle\hat{\rho}\rangle$, where N is the density of atoms). We then have the relation $N\langle\hat{\rho}\rangle = \epsilon_0\chi\mathbf{E}$, from which we can solve for χ .

After we derive the susceptibility, we demonstrate how the absorption and dispersion change as a function of various parameters, predicting what our experiment will reveal.

1.2 Deriving the EIT Hamiltonian

The system under investigation is a three level Λ atom, consisting of the eigenstates $|1\rangle$, $|2\rangle$ and $|3\rangle$, with corresponding eigenvalue energies $\hbar\omega_n$. We have labeled the states in order of increasing energy, where $|1\rangle$ is a stable ground state, $|2\rangle$ is a meta stable state, and both are coupled to the excited state $|3\rangle$.

We will write the Hamiltonian in the form

$$H = H_0 + H_1, \tag{1.2}$$

where H_0 is the Hamiltonian describing the free atom without external fields, and H_1 is the perturbation due to the applied electric field. H_0 and its eigenvectors account for all the interactions between the nucleus and electron.

As we are making the assumption that we only have three states, we can form a

complete orthonormal basis consisting of the three states $|n\rangle$, each with a corresponding eigenvalue of $\hbar\omega_n$. Completeness and orthonormality give:

$$\sum_n |n\rangle\langle n| = 1, \quad \langle n|m\rangle = \delta_{nm}. \quad (1.3)$$

Employing these eigenvectors and the eigenvalues, we may write the unperturbed Hamiltonian in terms of states $|n\rangle$ as:

$$H_0 = \left(\sum_n |n\rangle\langle n| \right) H \left(\sum_n |n\rangle\langle n| \right) = \begin{bmatrix} \hbar\omega_1 & 0 & 0 \\ 0 & \hbar\omega_2 & 0 \\ 0 & 0 & \hbar\omega_3 \end{bmatrix}. \quad (1.4)$$

We will now be perturbing H_0 with an electric field. The $|2\rangle \rightarrow |3\rangle$ transition is driven by a strong control field of amplitude \mathcal{E}_c and frequency ω_c , while the $|1\rangle \rightarrow |3\rangle$ transition is driven by a weak probe field of amplitude \mathcal{E}_p and frequency ω_p . The $|1\rangle \rightarrow |2\rangle$ transition is assumed to be a dipole forbidden transition. All other energy levels are assumed to be sufficiently off resonance for other transitions to be negligible.

The applied electric field can thus be written as

$$\mathbf{E} = \mathcal{E}_p \cos(\omega_p t - \mathbf{k}_p \cdot \mathbf{r}) + \mathcal{E}_c \cos(\omega_c t - \mathbf{k}_c \cdot \mathbf{r}), \quad (1.5)$$

where \mathbf{k} are the wave vectors associated with ω . For incident light with wavelengths much longer than the effective radius of the atom, $\lambda \gg r$, the spatial component can be dropped². This can be seen by a trigonometric identity:

$$\cos(\omega t - \mathbf{k} \cdot \mathbf{r}) = \cos(\omega t) \cos(-\mathbf{k} \cdot \mathbf{r}) - \sin(\omega t) \sin(-\mathbf{k} \cdot \mathbf{r}). \quad (1.6)$$

When $\lambda \gg r$ we have $1 \gg k \cdot r$, and $\cos(\mathbf{k} \cdot \mathbf{r}) \sim 1$, $\sin(\mathbf{k} \cdot \mathbf{r}) \sim 0$. The electric field becomes

$$\mathbf{E} = \mathcal{E}_p \cos(\omega_p t) + \mathcal{E}_c \cos(\omega_c t). \quad (1.7)$$

The energy of this perturbation will be given by

$$H_1 = -q\mathbf{E} \cdot \hat{\mathbf{r}}, \quad (1.8)$$

where q is the electron charge, \mathbf{E} is the classical vector valued electric field, and $\hat{\mathbf{r}}$

²This is a good approximation for visible light ($\lambda \sim 10^{-7}\text{m}$ compared to the Bohr radius $a_0 \sim 10^{-10}\text{m}$)

is the position operator. The term $-q\mathbf{E} \cdot \hat{\mathbf{r}}$, is simply the energy associated with a dipole of charge q and separation vector $\hat{\mathbf{r}}$ in the applied field \mathbf{E} . Thus, the assumption $\lambda \gg r$ is known as the dipole approximation.

Assuming the dipole is aligned with the electric field, we have:

$$H_1 = -qE\hat{r}. \quad (1.9)$$

We now will define the dipole moment operator as $\wp = q\hat{r}$, and the elements of the operator in the eigenbasis of H_0 by $\wp_{nm} = \wp_{mn}^* = \langle n|\wp|m\rangle$. The perturbation becomes

$$H_1 = -\wp E = -\left(\sum_n |n\rangle\langle n|\right) \wp \left(\sum_n |n\rangle\langle n|\right) E = -E \begin{bmatrix} \wp_{11} & \wp_{12} & \wp_{13} \\ \wp_{21} & \wp_{22} & \wp_{23} \\ \wp_{31} & \wp_{32} & \wp_{33} \end{bmatrix}. \quad (1.10)$$

To simplify the dipole moment operator, we assume $\wp_{12} = \wp_{21} = 0$, consistent with the forbidden $|1\rangle \rightarrow |2\rangle$ transition. Additionally we assume $\wp_{ii} = 0$, removing all the diagonal elements. This amounts to assuming that the atoms have no permanent dipole moments, which is true for atoms with spherically symmetric wave functions [12]. This assumption holds for a variety of atomic materials, including Rubidium, our species of interest. Under these assumptions, we have:

$$H_1 = -E \begin{bmatrix} 0 & 0 & \wp_{13} \\ 0 & 0 & \wp_{23} \\ \wp_{31} & \wp_{32} & 0 \end{bmatrix}. \quad (1.11)$$

1.3 Rotating Wave Approximation

To find the EIT Hamiltonian, we will invoke the rotating wave approximation, which neglects any rapidly oscillating terms in the Hamiltonian. To reveal these terms, we must transform into the interaction picture using the time evolution operator:

$$U(t) = e^{iH_0 t/\hbar} = \begin{bmatrix} e^{i\omega_1 t} & 0 & 0 \\ 0 & e^{i\omega_2 t} & 0 \\ 0 & 0 & e^{i\omega_3 t} \end{bmatrix}. \quad (1.12)$$

Applying this transformation to H_1 gives³:

$$UH_1U^\dagger = -E \begin{bmatrix} 0 & 0 & \wp_{13}e^{i(\omega_1-\omega_3)t} \\ 0 & 0 & \wp_{23}e^{i(\omega_2-\omega_3)t} \\ \wp_{31}e^{i(\omega_3-\omega_1)t} & \wp_{32}e^{i(\omega_3-\omega_2)t} & 0 \end{bmatrix}. \quad (1.13)$$

We now will want to substitute in the electric field, and expand the cosines in terms of exponentials:

$$E = \mathcal{E}_p \cos \omega_p t + \mathcal{E}_c \cos \omega_c t = \frac{\mathcal{E}_p}{2}(e^{i\omega_p t} + e^{-i\omega_p t}) + \frac{\mathcal{E}_c}{2}(e^{i\omega_c t} + e^{-i\omega_c t}). \quad (1.14)$$

The non-zero matrix elements are:

$$(UH_1U^\dagger)_{13} = -\wp_{13} \left(\frac{\mathcal{E}_p}{2}(e^{i\omega_p t} + e^{-i\omega_p t}) + \frac{\mathcal{E}_c}{2}(e^{i\omega_c t} + e^{-i\omega_c t}) \right) e^{i(\omega_1-\omega_3)t} \quad (1.15)$$

$$(UH_1U^\dagger)_{23} = -\wp_{23} \left(\frac{\mathcal{E}_p}{2}(e^{i\omega_p t} + e^{-i\omega_p t}) + \frac{\mathcal{E}_c}{2}(e^{i\omega_c t} + e^{-i\omega_c t}) \right) e^{i(\omega_2-\omega_3)t} \quad (1.16)$$

$$(UH_1U^\dagger)_{31} = -\wp_{31} \left(\frac{\mathcal{E}_p}{2}(e^{i\omega_p t} + e^{-i\omega_p t}) + \frac{\mathcal{E}_c}{2}(e^{i\omega_c t} + e^{-i\omega_c t}) \right) e^{i(\omega_3-\omega_1)t} \quad (1.17)$$

$$(UH_1U^\dagger)_{23} = -\wp_{23} \left(\frac{\mathcal{E}_p}{2}(e^{i\omega_p t} + e^{-i\omega_p t}) + \frac{\mathcal{E}_c}{2}(e^{i\omega_c t} + e^{-i\omega_c t}) \right) e^{i(\omega_2-\omega_3)t} \quad (1.18)$$

We now apply the rotating wave approximation, which amounts to assuming that any quickly oscillating term will be averaged out on the time scale of observation. Recall that ω_p is near resonance with the $\omega_3 \rightarrow \omega_1$ transition, so the difference $\omega_3 - \omega_1 - \omega_p$ will be small, and any exponentials with these terms will remain since they oscillate slowly. However, terms containing the sum $\omega_3 - \omega_1 + \omega_p$ will be large, and so these quickly oscillating terms can be dropped in the rotating wave approximation. Similar reasoning is applied to all terms. Only one term of four in each matrix element survives:

$$(UH_1U^\dagger)_{13} = -\frac{1}{2}\mathcal{E}_p\wp_{13}e^{i(\omega_1-\omega_3+\omega_p)t} \quad (1.19)$$

$$(UH_1U^\dagger)_{23} = -\frac{1}{2}\mathcal{E}_c\wp_{23}e^{i(\omega_2-\omega_3+\omega_c)t} \quad (1.20)$$

$$(UH_1U^\dagger)_{31} = -\frac{1}{2}\mathcal{E}_p\wp_{31}e^{i(\omega_3-\omega_1-\omega_p)t} \quad (1.21)$$

$$(UH_1U^\dagger)_{32} = -\frac{1}{2}\mathcal{E}_c\wp_{32}e^{i(\omega_3-\omega_2-\omega_c)t} \quad (1.22)$$

³We could apply this transformation to H in its entirety, but H_0 is unaffected by the transformation as it is diagonal, and so bringing it along for the ride is unnecessary.

We can now reverse this transformation again applying the $U(t)$ transform to return to the Schrödinger picture.

$$H_1 = -\frac{1}{2} \begin{bmatrix} 0 & 0 & \wp_{13}\mathcal{E}_p e^{i\omega_p t} \\ 0 & 0 & \wp_{23}\mathcal{E}_c e^{i\omega_c t} \\ \wp_{31}\mathcal{E}_p e^{-i\omega_p t} & \wp_{32}\mathcal{E}_c e^{-i\omega_c t} & 0 \end{bmatrix}. \quad (1.23)$$

It is sensible for us to write the Hamiltonian in terms of the Rabi frequencies. First, let us separate the dipole operator into magnitude and phase:

$$\wp_{13} = \wp_{31}^* = |\wp_{13}| e^{i\phi_p}, \quad (1.24)$$

$$\wp_{23} = \wp_{32}^* = |\wp_{23}| e^{i\phi_c}. \quad (1.25)$$

Now define the Rabi frequencies:

$$\Omega_p = \frac{\mathcal{E}_p |\wp_{13}|}{\hbar}, \quad (1.26)$$

$$\Omega_c = \frac{\mathcal{E}_c |\wp_{23}|}{\hbar}. \quad (1.27)$$

This gives us:

$$H_1 = -\frac{\hbar}{2} \begin{bmatrix} 0 & 0 & \Omega_p e^{i\phi_p} e^{i\omega_p t} \\ 0 & 0 & \Omega_c e^{i\phi_c} e^{i\omega_c t} \\ \Omega_p e^{-i\phi_p} e^{-i\omega_p t} & \Omega_c e^{-i\phi_c} e^{-i\omega_c t} & 0 \end{bmatrix}. \quad (1.28)$$

Combining H_0 and H_1 , we have the complete EIT Hamiltonian:

$$H_{EIT} = \frac{\hbar}{2} \begin{bmatrix} 2\omega_1 & 0 & -\Omega_p e^{i\phi_p} e^{i\omega_p t} \\ 0 & 2\omega_2 & -\Omega_c e^{i\phi_c} e^{i\omega_c t} \\ -\Omega_p e^{-i\phi_p} e^{-i\omega_p t} & -\Omega_c e^{-i\phi_c} e^{-i\omega_c t} & 2\omega_3 \end{bmatrix}. \quad (1.29)$$

1.4 Corotating Frame

While the previous transformation made clear the simplifications of the rotating wave approximation, the next transformation we apply is constructed to remove all time dependence from the Hamiltonian, as well as the phase of the dipole moment operator. This new basis is known as the rotating basis, which we will denote with $\tilde{\sim}$'s on transformed elements. The new basis $|\tilde{n}\rangle$ is related to the old by $|\tilde{n}\rangle = \tilde{U}(t)|n\rangle$ where

\tilde{U} is given by:

$$\tilde{U}(t) = \begin{bmatrix} e^{-i\omega_p t} e^{-i\phi_p} & 0 & 0 \\ 0 & e^{-i\omega_c t} e^{-i\phi_c} & 0 \\ 0 & 0 & 1 \end{bmatrix}. \quad (1.30)$$

For this transformation to be sensible, it must be unitary. It clearly is. The transformed Hamiltonian also satisfies the Schrödinger equation:

$$\tilde{H}_{EIT}|\tilde{n}\rangle = i\hbar \frac{\partial}{\partial t} |\tilde{n}\rangle \quad (1.31)$$

$$= i\hbar \frac{\partial}{\partial t} (\tilde{U}|n\rangle) \quad (1.32)$$

$$= i\hbar \left(\frac{\partial \tilde{U}}{\partial t} |n\rangle + \tilde{U} \frac{\partial |n\rangle}{\partial t} \right) \quad (1.33)$$

$$= i\hbar \left(\frac{\partial \tilde{U}}{\partial t} |n\rangle + \frac{-i}{\hbar} \tilde{U} H_{EIT} |n\rangle \right) \quad (1.34)$$

$$= \left(i\hbar \frac{\partial \tilde{U}}{\partial t} \tilde{U}^\dagger + \tilde{U} H_{EIT} \tilde{U}^\dagger \right) \tilde{U} |n\rangle \quad (1.35)$$

$$\tilde{H}_{EIT}|\tilde{n}\rangle = \left(i\hbar \frac{\partial \tilde{U}}{\partial t} \tilde{U}^\dagger + \tilde{U} H_{EIT} \tilde{U}^\dagger \right) |\tilde{n}\rangle. \quad (1.36)$$

We find that the use of the transformation simplifies the Hamiltonian dramatically:

$$\tilde{H}_{EIT} = i\hbar \frac{\partial \tilde{U}}{\partial t} \tilde{U}^\dagger + \tilde{U} H_{EIT} \tilde{U}^\dagger \quad (1.37)$$

$$= \frac{\hbar}{2} \begin{bmatrix} 2\omega_p & 0 & 0 \\ 0 & 2\omega_c & 0 \\ 0 & 0 & 0 \end{bmatrix} + \frac{\hbar}{2} \begin{bmatrix} 2\omega_1 & 0 & -\Omega_p \\ 0 & 2\omega_2 & -\Omega_c \\ -\Omega_p & -\Omega_c & 2\omega_3 \end{bmatrix} \quad (1.38)$$

$$\tilde{H}_{EIT} = \frac{\hbar}{2} \begin{bmatrix} 2(\omega_1 + \omega_p) & 0 & -\Omega_p \\ 0 & 2(\omega_2 + \omega_c) & -\Omega_c \\ -\Omega_p & -\Omega_c & 2\omega_3 \end{bmatrix}. \quad (1.39)$$

\tilde{H}_{EIT} no longer contains any time dependent terms. We can bring the Hamiltonian into its standard form[7] by noting that we can add a multiple of the identity to the Hamiltonian without changing any physical results⁴. Adding $-2(\omega_1 + \omega_p)\mathbf{1}$ to the

⁴We will effectively be redefining our eigenvalues by setting $\omega_n \rightarrow \omega_n + A$ for some constant A . This has no physical effect, as the physically relevant terms are the *differences* between energy levels.

Hamiltonian gives

$$\tilde{H}_{EIT} = \frac{\hbar}{2} \begin{bmatrix} 0 & 0 & -\Omega_p \\ 0 & 2(\omega_2 + \omega_c - \omega_1 - \omega_p) & -\Omega_c \\ -\Omega_p & -\Omega_c & 2(\omega_3 - \omega_1 - \omega_p) \end{bmatrix}. \quad (1.40)$$

Defining the laser detunings as $\Delta_p = \omega_p - \omega_3 + \omega_1$ and $\Delta_c = \omega_c - \omega_3 + \omega_2$, we arrive at

$$\tilde{H}_{EIT} = -\frac{\hbar}{2} \begin{bmatrix} 0 & 0 & \Omega_p \\ 0 & 2(\Delta_p - \Delta_c) & \Omega_c \\ \Omega_p & \Omega_c & 2\Delta_p \end{bmatrix}. \quad (1.41)$$

This clever time independent Hamiltonian allows for a simplified solution procedure when we solve the equations of motion.

In order to properly analyze this Hamiltonian, we will want to introduce some additional tools, namely, the density operator and the von Neumann Equation.

1.5 Density Operators

The Hamiltonian \tilde{H}_{EIT} describes a single atom system and the corresponding Schrödinger Equation governs its evolution in time. However, we will not in general know the specific state Ψ of the atom, and instead the atom will be in a mixed state, with a particular probability P_n of being in state $|n\rangle$ ⁵. An example of a mixed state, and the case of interest here, is an ensemble of single atom systems with distributions of states given by P_n .

Approaching this formally, we will assume a complete, orthonormal basis:

$$\sum_n |n\rangle\langle n| = 1, \quad \langle n|m\rangle = \delta_{nm}. \quad (1.42)$$

And we will define the density operator:

$$\rho = \sum_n P_n |n\rangle\langle n|. \quad (1.43)$$

Now, we can see that the expectation value of a Hermitian operator (representing

⁵Note that a mixed state is *not* the same as a quantum superposition of pure states, $\Psi = c_1|1\rangle + c_2|2\rangle$, for the superposition Ψ is also a pure quantum state. A mixed state is a result of *classical* uncertainty in the preparation of the system, not the inherent quantum uncertainty from the measurement of a quantum value.

an observable) for an unknown state is given by

$$\langle \mathcal{O} \rangle = \sum_n P_n \langle n | \mathcal{O} | n \rangle, \quad (1.44)$$

where we are summing over all states, and P_n is the probability that the system is in state n . Note that $\sum_n P_n = 1$, since the system must be in some state. Employing the newly defined density operator, we see that we can write the expectation value of the operator in a new way:

$$\langle \mathcal{O} \rangle = \sum_n P_n \langle n | \mathcal{O} | n \rangle \quad (1.45)$$

$$= \sum_m \sum_n P_n \langle n | \mathcal{O} | m \rangle \langle m | n \rangle \quad (1.46)$$

$$= \sum_m \sum_n P_n \langle m | n \rangle \langle n | \mathcal{O} | m \rangle \quad (1.47)$$

$$= \sum_m \langle m | \rho \mathcal{O} | m \rangle \quad (1.48)$$

$$\langle \mathcal{O} \rangle = \text{Tr}(\rho \mathcal{O}). \quad (1.49)$$

The expectation value of an operator \mathcal{O} is given by the trace of $\rho \mathcal{O}$. We now have a new method of generating expectation values using the density operator. In the next section we will continue further and transform the Schrödinger Equation to make no reference to the wave function, replacing it with ρ entirely.

1.6 The Von Neumann Equation

We can rewrite the Schrödinger Equation in terms of the density operator, where the density operator will ultimately replace the wave function. The Schrödinger equation and its conjugate are:

$$\langle \dot{\psi} | = \frac{i}{\hbar} \langle \psi | H, \quad | \dot{\psi} \rangle = -\frac{i}{\hbar} H | \psi \rangle. \quad (1.50)$$

We now take the time derivative of the density operator

$$\rho = \sum_n P_n | n \rangle \langle n |, \quad (1.51)$$

and make a few substitutions to obtain the von Neumann Equation:

$$\dot{\rho} = P_n \sum_n |\dot{n}\rangle\langle n| + |n\rangle\langle\dot{n}| \quad (1.52)$$

$$= -\frac{i}{\hbar} \sum_n HP_n|n\rangle\langle n| - P_n|n\rangle\langle n|H \quad (1.53)$$

$$= -\frac{i}{\hbar}(H\rho - \rho H) \quad (1.54)$$

$$\dot{\rho} = -\frac{i}{\hbar}[H, \rho]. \quad (1.55)$$

The von Neumann Equation is equivalent to the Schrödinger equation, but has the benefit that it makes no reference to pure states, which we often do not know *a priori*.

Quantum systems are generally much more complicated than is feasible to include in our models - such complexities include interactions and collisions between atoms, and spontaneous emission and decays. Each of these processes removes population from a given state. To account for these effects, we add in phenomenological decay terms⁶:

$$\dot{\rho} = -\frac{i}{\hbar}[H, \rho] - \frac{1}{2}\{\Gamma, \rho\}. \quad (1.56)$$

Where Γ is defined by:

$$\langle n|\Gamma|m\rangle = \gamma_n\delta_{nm}. \quad (1.57)$$

These added terms account for decays from each state for a general set of energy levels, but in a Λ system matters simplify. Firstly, γ_1 will drop to zero, since conservation of energy prevents relaxations out of the ground state. Secondly, since $|2\rangle$ is a metastable state, γ_2 will be dramatically smaller than γ_3 . We shall see in Section 1.9 that the long lifetime of $|2\rangle$ is essential for maintaining coherence and EIT. These decay rates are shown in Fig. 1.2.

We can also write the von Neumann Equation in component form, which we will use in the next section:

$$\dot{\rho}_{ij} = -\frac{i}{\hbar} \sum_k \left[(H_{ik}\rho_{kj} - \rho_{ik}H_{kj}) + \frac{1}{2}(\Gamma_{ik}\rho_{kj} + \rho_{ik}\Gamma_{kj}) \right]. \quad (1.58)$$

⁶The anti-commutator is defined as $\{A, B\} = AB + BA$.

1.7 Solving for the Density Matrix Elements

Now that we have the simplified EIT Hamiltonian in the rotating basis (Eq. (1.29)), we can generate the equations of motion for the density operators using the von Neumann Equation, Eq. (1.58). We saw in Section 1.4 that the Schrödinger equation holds in the new basis, and so, as they are equivalent, the von Neumann Equation also holds for $\tilde{\rho}$ and \tilde{H}_{EIT} . The diagonal matrix elements are given by:

$$\begin{aligned}\dot{\rho}_{11} &= i\frac{\Omega_p}{2}(\rho_{21} - \rho_{12}) \\ \dot{\rho}_{22} &= -\gamma_2\rho_{22} - i\frac{\Omega_p}{2}(\rho_{21} - \rho_{12}) - i\frac{\Omega_c}{2}(\rho_{23} - \rho_{32}) \\ \dot{\rho}_{33} &= -\gamma_3\rho_{33} + i\frac{\Omega_c}{2}(\rho_{23} - \rho_{32})\end{aligned}\quad (1.59)$$

It is important to note that the γ decay terms remove atoms from our population entirely. This aspect is undesired, since decays from $|2\rangle$ and $|3\rangle$ would not actually leave our system, but would instead decay to $|1\rangle$. We can fix this issue by noting that our system is being pumped into $|1\rangle$ by the action of the strong control beam. As long as our probe beam is weak, the atoms will primarily inhabit the $|1\rangle$ state in steady state solutions. This strong control beam assumption makes our system essentially conservative, allowing us to interpret the diagonal elements ρ_{ii} as the fraction of atoms in our ensemble that are in state $|i\rangle$ [12].

The off-diagonal elements are given by:

$$\begin{aligned}\dot{\rho}_{21}^* &= \dot{\rho}_{12} = (-\gamma_{12} + i(\Delta_c - \Delta_p))\tilde{\rho}_{12} - i\frac{\Omega_c}{2}\tilde{\rho}_{13} + i\frac{\Omega_p}{2}\tilde{\rho}_{32} \\ \dot{\rho}_{31}^* &= \dot{\rho}_{13} = (-\gamma_{13} - i\Delta_p)\tilde{\rho}_{13} + i\frac{\Omega_p}{2}(\tilde{\rho}_{33} - \tilde{\rho}_{11}) - i\frac{\Omega_c}{2}\tilde{\rho}_{12} \\ \dot{\rho}_{32}^* &= \dot{\rho}_{23} = (-\gamma_{23} - i\Delta_c)\tilde{\rho}_{23} + i\frac{\Omega_c}{2}(\tilde{\rho}_{33} - \tilde{\rho}_{22}) - i\frac{\Omega_p}{2}\tilde{\rho}_{21}\end{aligned}\quad (1.60)$$

Here we have defined the off-diagonal decay rates $\gamma_{ab} = \frac{1}{2}(\gamma_a + \gamma_b)$. The $*$'s represent complex conjugates. We can use the assumption of a strong control beam to simplify these equations. As we mentioned, the atoms will primarily be in the ground state $|1\rangle$, with few atoms in the excited states. This allows us to write⁷:

$$\rho_{11} \approx 1, \quad \rho_{22} = \rho_{33} \approx 0. \quad (1.61)$$

⁷This still allows transitions from the ground state to the excited state, we are only asserting that the excited population is negligible.

Substituting this approximation in gives:

$$\begin{aligned}
\dot{\tilde{\rho}}_{21}^* &= \dot{\tilde{\rho}}_{12} = (-\gamma_{12} + i(\Delta_c - \Delta_p))\tilde{\rho}_{12} - i\frac{\Omega_c}{2}\tilde{\rho}_{13} + i\frac{\Omega_p}{2}\tilde{\rho}_{32} \\
\dot{\tilde{\rho}}_{31}^* &= \dot{\tilde{\rho}}_{13} = (-\gamma_{13} - i\Delta_p)\tilde{\rho}_{13} - i\frac{\Omega_p}{2} - i\frac{\Omega_c}{2}\tilde{\rho}_{12} \\
\dot{\tilde{\rho}}_{32}^* &= \dot{\tilde{\rho}}_{23} = (-\gamma_{23} - i\Delta_c)\tilde{\rho}_{23} - i\frac{\Omega_p}{2}\tilde{\rho}_{21}
\end{aligned} \tag{1.62}$$

The weak probe assumption also allows us to drop any terms proportional to Ω_p^2 , because Ω_p is proportional to our probe beam electric field magnitude \mathcal{E}_p . Looking at steady state solutions (where time derivatives vanish), we observe that $\tilde{\rho}_{23}$ is first order in Ω_p . Thus, the term $i\frac{\Omega_p}{2}\tilde{\rho}_{32}$ is second order in Ω_p , and can be dropped under the approximation. We now have a nice coupled pair of equations:

$$\begin{aligned}
\dot{\tilde{\rho}}_{21}^* &= \dot{\tilde{\rho}}_{12} = (-\gamma_{12} + i(\Delta_c - \Delta_p))\tilde{\rho}_{12} - i\frac{\Omega_c}{2}\tilde{\rho}_{13}, \\
\dot{\tilde{\rho}}_{31}^* &= \dot{\tilde{\rho}}_{13} = (-\gamma_{13} - i\Delta_p)\tilde{\rho}_{13} - i\frac{\Omega_p}{2} - i\frac{\Omega_c}{2}\tilde{\rho}_{12}.
\end{aligned}$$

This can be solved as a matrix equation - first define:

$$\mathbf{X} = \begin{bmatrix} \tilde{\rho}_{12} \\ \tilde{\rho}_{13} \end{bmatrix}, \quad \mathbf{M} = \begin{bmatrix} -\gamma_{12} + i(\Delta_c - \Delta_p) & -i\frac{\Omega_c}{2} \\ -i\frac{\Omega_c}{2} & -\gamma_{13} - i\Delta_p \end{bmatrix}, \quad \mathbf{A} = \begin{bmatrix} 0 \\ -i\frac{\Omega_p}{2} \end{bmatrix}.$$

The system of equations can be written as:

$$\dot{\mathbf{X}} = \mathbf{M} \cdot \mathbf{X} + \mathbf{A}. \tag{1.63}$$

This has the steady state solution (for $\dot{\mathbf{X}} = 0$) of:

$$\mathbf{X} = -\mathbf{M}^{-1}\mathbf{A}. \tag{1.64}$$

This is a stable solution because the eigenvalues of \mathbf{M} have negative real components⁸, which correspond to solutions involving decaying exponentials. Thus, the system will approach this solution as $t \rightarrow \infty$. Computing this term gives the following

⁸This is easily verifiable for $\Delta_c = 0$, and also holds for expansions for small Δ_c . It was not verified for large Δ_c , though we expect EIT to not be apparent for sufficiently large detuning anyway.

components of \mathbf{X} :

$$\tilde{\rho}_{12} = \frac{\Omega_c \Omega_p}{4(i\gamma_{12} + \Delta_c - \Delta_p)(-i\gamma_{13} + \Delta_p) + \Omega_c^2}, \quad (1.65)$$

$$\tilde{\rho}_{13} = -\frac{2(\gamma_{12} - i(\Delta_c - \Delta_p))\Omega_p}{4(\gamma_{13} + i\Delta_p)(-i\gamma_{12} - \Delta_c + \Delta_p) - i\Omega_c^2}. \quad (1.66)$$

1.8 From Density to Susceptibility

We have derived the functional form of the density operators that are associated with energy level transitions. We will see in this section that ρ_{13} determines the susceptibility of the medium as seen by the probe.

The polarization of a medium is defined as the dipole moment per unit volume - if we let N be the number of atoms per unit volume, the polarization can be expressed in terms of the expectation of the dipole operator:

$$\mathbf{P} = N\langle\wp\rangle = N\text{Tr}(\rho\wp). \quad (1.67)$$

Expanding the trace, we get:

$$\mathbf{P} = N\text{Tr} \left(\begin{bmatrix} \rho_{11} & \rho_{12} & \rho_{13} \\ \rho_{21} & \rho_{22} & \rho_{23} \\ \rho_{31} & \rho_{32} & \rho_{33} \end{bmatrix} \begin{bmatrix} 0 & 0 & \wp_{13} \\ 0 & 0 & \wp_{23} \\ \wp_{31} & \wp_{32} & 0 \end{bmatrix} \right) \quad (1.68)$$

$$= N(\wp_{31}\rho_{13} + \wp_{32}\rho_{23} + \wp_{13}\rho_{31} + \wp_{23}\rho_{32}). \quad (1.69)$$

We computed the density matrix elements in Section 1.7, but they were in the rotating basis. We can convert these elements in the regular basis by using the inverse transformation $\rho = \tilde{U}^\dagger \tilde{\rho} \tilde{U}$ ⁹:

$$\begin{bmatrix} \rho_{11} & \rho_{12} & \rho_{13} \\ \rho_{21} & \rho_{22} & \rho_{23} \\ \rho_{31} & \rho_{32} & \rho_{33} \end{bmatrix} = \begin{bmatrix} \tilde{\rho}_{11} & \tilde{\rho}_{12} e^{i(\omega_p - \omega_c)t} e^{-i\phi_c} e^{i\phi_p} & \tilde{\rho}_{13} e^{i\omega_p t} e^{i\phi_p} \\ \tilde{\rho}_{21} e^{i(-\omega_p + \omega_c)t} e^{i\phi_c} e^{-i\phi_p} & \tilde{\rho}_{22} & \tilde{\rho}_{23} e^{i\omega_c t} e^{i\phi_c} \\ \tilde{\rho}_{31} e^{-i\omega_p t} e^{-i\phi_p} & \tilde{\rho}_{32} e^{-i\omega_c t} e^{-i\phi_c} & \tilde{\rho}_{33} \end{bmatrix}. \quad (1.70)$$

We can now write the polarization from Eq. (1.69) in terms of the known $\tilde{\rho}$ density matrix elements:

$$\mathbf{P} = N(\wp_{31}\tilde{\rho}_{13} e^{i\omega_p t} e^{i\phi_p} + \wp_{32}\tilde{\rho}_{23} e^{i\omega_c t} e^{i\phi_c} + \wp_{13}\tilde{\rho}_{31} e^{-i\omega_p t} e^{-i\phi_p} + \wp_{23}\tilde{\rho}_{32} e^{-i\omega_c t} e^{-i\phi_c}). \quad (1.71)$$

Remembering that we are looking for the linear susceptibility χ , given by the

⁹The density operator clearly transforms this way from the definition of the operator in Eq. (1.43)

relation $\mathbf{P} = \epsilon_0 \chi \mathbf{E}$, and writing the electric field from Eq. (1.7) in full, we have¹⁰:

$$\mathbf{P} = \epsilon_0 \chi \mathbf{E} = \chi(\omega_p) \frac{\epsilon_0 \mathcal{E}_p}{2} (e^{i\omega_p t} + e^{-i\omega_p t}) + \chi_c(\omega_c) \frac{\epsilon_0 \mathcal{E}_c}{2} (e^{i\omega_c t} + e^{-i\omega_c t}). \quad (1.72)$$

From these last two equations, we can match the time dependent exponentials, giving us:

$$N \wp_{31} \tilde{\rho}_{13} e^{i\omega_p t} e^{i\phi_p} = \chi(\omega_p) \frac{\epsilon_0 \mathcal{E}_p}{2} e^{i\omega_p t}. \quad (1.73)$$

Solving for χ , we have:

$$\chi = \frac{2N \wp_{31}}{\mathcal{E}_p \epsilon_0} \tilde{\rho}_{13} e^{i\phi_p}. \quad (1.74)$$

Replacing $\wp_{31} = |\wp_{13}| e^{-i\phi_p}$ from Eq. (1.24) we have:

$$\chi = \frac{2N |\wp_{13}|}{\mathcal{E}_p \epsilon_0} \tilde{\rho}_{13}. \quad (1.75)$$

Adding in the solution for $\tilde{\rho}_{13}$ from Eq. (1.65), the final equation for the linear susceptibility is given by

$$\chi = \frac{2N |\wp_{13}| \Omega_p}{\mathcal{E}_p \epsilon_0} \frac{-2(\gamma_{12} + i(\Delta_c - \Delta_p)) \Omega_p}{4(\gamma_{13} - i\Delta_p)(+i\gamma_{12} - \Delta_c + \Delta_p) + i\Omega_c^2}. \quad (1.76)$$

We now will split χ into real and imaginary components. After simplification, these are:

$$\text{Re}(\chi) = -\frac{2N |\wp_{13}| \Omega_p}{\mathcal{E}_p \epsilon_0} \frac{2(4(\gamma_{12}^2 + (\Delta_c - \Delta_p)^2) \Delta_p + (\Delta_c - \Delta_p) \Omega_c^2)}{16(\gamma_{12}^2 + (\Delta_c - \Delta_p)^2)(\gamma_{13}^2 + \Delta_p^2) + 8(\gamma_{12} \gamma_{13} + (\Delta_c - \Delta_p) \Delta_p) \Omega_c^2 + \Omega_c^4} \quad (1.77)$$

$$\text{Im}(\chi) = \frac{2N |\wp_{13}| \Omega_p}{\mathcal{E}_p \epsilon_0} \frac{2(4\gamma_{13}(\gamma_{12}^2 + (\Delta_c - \Delta_p)^2) + \gamma_{12} \Omega_c^2)}{16(\gamma_{12}^2 + (\Delta_c - \Delta_p)^2)(\gamma_{13}^2 + \Delta_p^2) + 8(\gamma_{12} \gamma_{13} + (\Delta_c - \Delta_p) \Delta_p) \Omega_c^2 + \Omega_c^4} \quad (1.78)$$

We can also see that for $\Omega_c = 0$, these equations reduce to a typical Lorentzian curve:

$$\text{Re}(\chi) = -\frac{N |\wp_{13}| \Omega_p}{\mathcal{E}_p \epsilon_0} \frac{\Delta_p}{\Delta_p^2 + \gamma_{13}^2}, \quad (1.79)$$

$$\text{Im}(\chi) = \frac{N |\wp_{13}| \Omega_p}{\mathcal{E}_p \epsilon_0} \frac{\gamma_{13}}{\Delta_p^2 + \gamma_{13}^2}. \quad (1.80)$$

¹⁰The susceptibility is frequency dependent, and since each of the applied fields has a distinct frequency, we have two distinct χ .

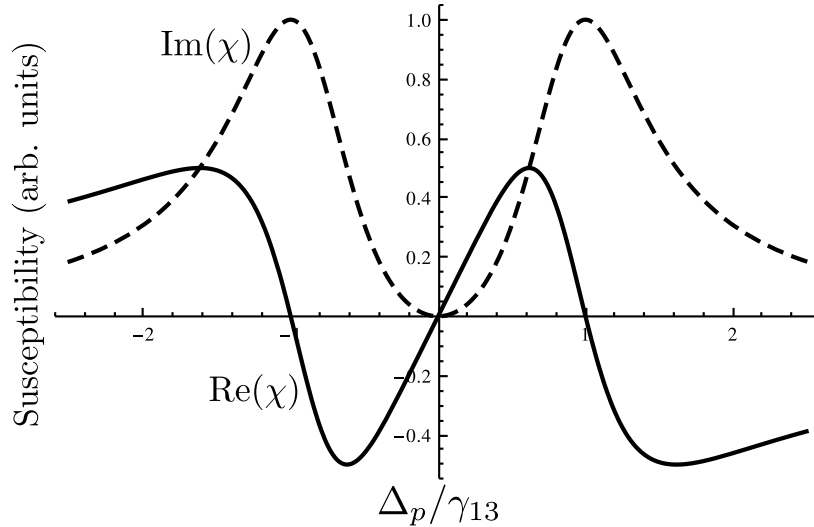


Figure 1.3: Electric susceptibility demonstrating EIT. This figure shows the electric susceptibility plotted as a function of normalized probe detuning. Normalization refers to plotting in units γ_{13} , which is the defining parameter of the Lorentzian peaks that normally occur for a resonance (see Eq. (1.80)). For this plot, control laser detuning $\Delta_c = 0$, the metastable state $|2\rangle$ is given a decay rate $\gamma_{12} = 10^{-4}\gamma_{13}$, the coupling strength is set to $\Omega_c = 2\gamma_{13}$.

1.9 Qualitative Predictions

We have determined the frequency dependence of the electric susceptibility. The imaginary and real components are plotted in Fig. 1.3 as a function of the probe detuning. The characteristic transparency at resonance is clearly visible, as is the steeper dispersion. In practice, it is terribly difficult to determine the Rabi frequencies and dipole moments. While the other constants usually can be determined, some are highly dependent on the physical setup. Because of this, the plots shown in this section use sensible but non-specific choices to predict the qualitative nature of EIT.

The onset of EIT is demonstrated in Fig. 1.4. The system is probed initially with zero control laser strength, which reveals a normal Lorentzian peak. As we increase the control laser power, a dip immediately appears. For stronger powers, the width of the transparency window increases significantly.

We mentioned that EIT requires $|2\rangle$ to be a metastable state, but now we can explicitly probe what happens as we increase the decay rate γ_{12} of the state $|2\rangle$. We expect that the interference between the excitation pathways will be reduced, since it relies on the transition rate that couples $|2\rangle \rightarrow |3\rangle$ to be much higher than the decay rate ($\Omega_c \gg \gamma_{12}$). Once we break this assumption, the destructive interference is reduced. This behavior is shown in Fig. 1.5.

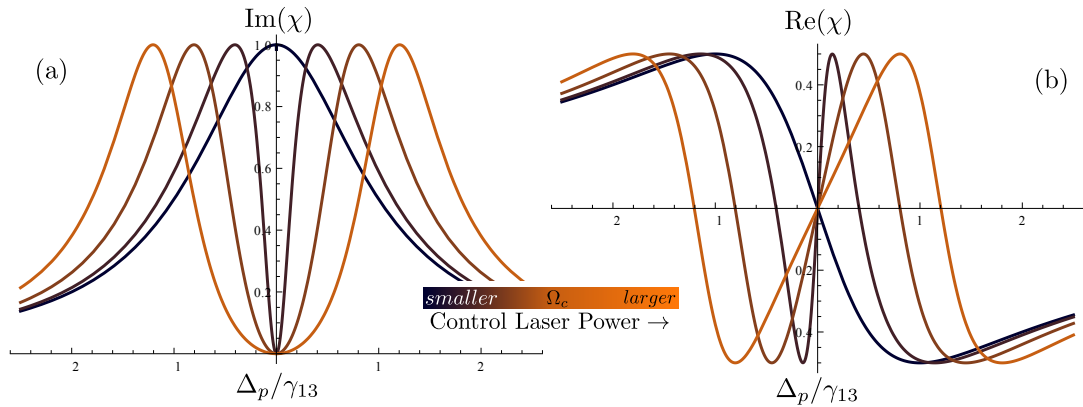


Figure 1.4: EIT and control laser power. This plot shows how the real (a) and imaginary (b) components of χ vary as we increase Ω_c . The first onset of EIT is very dramatic with a very thin transparency window and a very steep dispersion relation. As we increase Ω_c , the transparency widens and the dispersion becomes less steep.

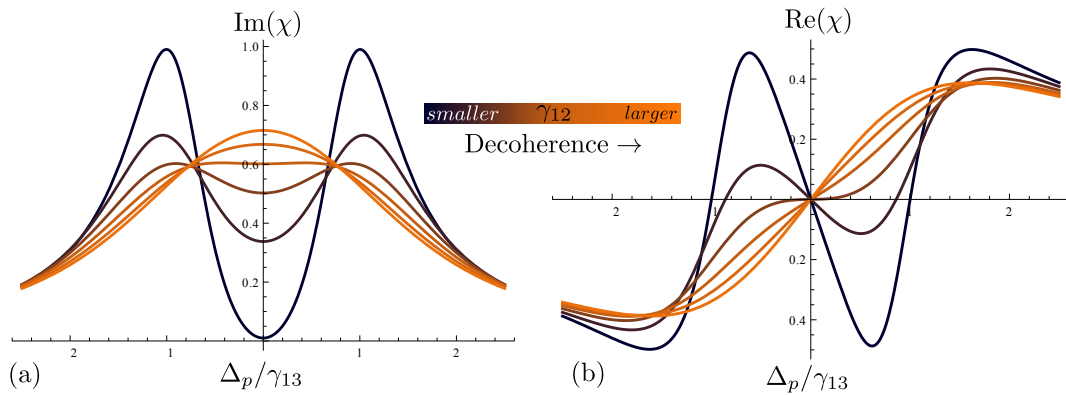


Figure 1.5: EIT and increasing decoherence. This plot shows how the real (a) and imaginary (b) components of χ vary as we increase γ_{12} . When γ_{12} is small, we see the EIT effects, but as we increase it they diminish gradually. When γ_{12} is large enough, the resonance becomes indistinguishable from a normal atomic resonance.

So far we have derived EIT for an ensemble of stationary atoms. However, we will be experimentally observing EIT in a system of thermal atoms with a Maxwell-Boltzmann velocity distribution. For a population of atoms moving at speed v , the observed frequency of incident light will be Doppler shifted. The atom will “see” a frequency changed by an amount

$$\Delta = v \frac{\omega}{c}, \quad (1.81)$$

where ω is the frequency of the incident laser light, and c is the speed of light in the medium. Note that we have two input frequencies, ω_c and ω_p , which are Doppler shifted by different amounts. However, as ω_c and ω_p are on the order of 10^{14} Hz, while the difference between them is only ~ 6.8 GHz, the Doppler frequency shift will effectively be the same, which we will call Δ .

If we choose to have the probe and control lasers copropagating (as we will in our experiment), then both the probe and control beams will be Doppler shifted in the same direction. To find the electric susceptibility of a selection of atoms moving at speed v , we simply replace Δ_p with $\Delta_p + \Delta$ and Δ_c with $\Delta_c + \Delta$ in Eq. (1.78). This substitution is plotted in Fig. 1.6 for several values of Δ ¹¹. We also have scaled each velocity group by a Maxwell-Boltzmann velocity distribution (a Gaussian distribution given by: $\exp\left[-\frac{\Delta^2}{(25)\gamma_{13}^2}\right]$). Observing the plot, we see that for each velocity group, there is still a full transparency at zero probe detuning. Thus, even for a Doppler broadened medium at room temperature, we expect to see a complete transparency at zero probe detuning.

This was verified further by numerically integrating over a complete Maxwell-Boltzmann distribution of atoms, shown in Fig. 1.7. This plot is the behavior we expect to see for a Doppler broadened medium, which is what we perform our experiment with, as we describe in Chapter 2.

¹¹We chose Δ to be integer multiples $n\gamma_{13}$ for all integers n in the range 0 to 5.

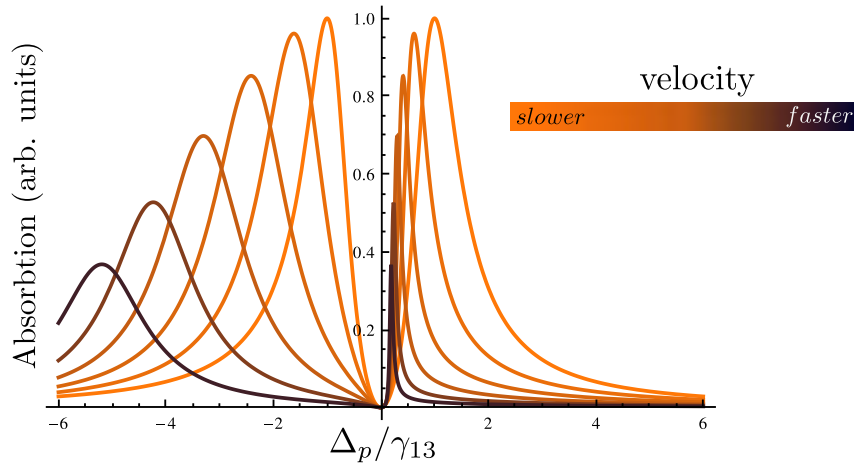


Figure 1.6: EIT Doppler broadened for selected velocities. This plot shows the electric susceptibility for populations of atoms moving at non-zero velocity, which “see” a frequency shifted probe and control laser. The control and probe are assumed to be copropagating, which amounts to adding some Doppler-shift Δ to both Δ_p and Δ_c in Eq. (1.78). Additionally, the relative magnitude of the susceptibilities for different velocities shown is assuming a Boltzmann distribution of velocities. One can see that even though the lasers are Doppler shifted, we still obtain a complete transparency at $\Delta_p = 0$. Note that other parameters are chosen to be the same as in Fig. 1.3.

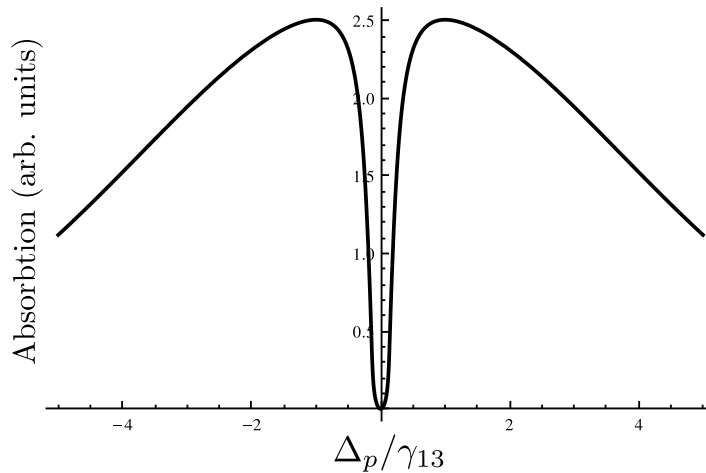


Figure 1.7: EIT Doppler broadened with numerical integration. This plot demonstrates that full transparency is achievable even for a Doppler broadened medium. The functional form and chosen values are the same as in Fig. 1.6, but we integrate over the velocity distribution rather than plot selected velocity groups. This is evidence that we should be capable of observing EIT.

Chapter 2

Experimental Setup

The essence of the experiment is straightforward: we want to take an absorption spectrum of a suitable Λ atom sample by scanning the frequency of a probe laser and measuring the probe transmittance using a photodiode. The process is to be repeated with and without an applied control laser, directly observing any EIT effects.

2.1 Atomic Structure of Rubidium

Rubidium is chosen as our atom species for a number of reasons: Most importantly for the purposes of EIT, it has a suitable atomic energy structure that can be used as an effective Λ scheme. Also important is that saturation absorption spectroscopy using rubidium is a very common technique and the primary components were already available in the lab. We choose the isotope ^{87}Rb , which has previously been used to demonstrate EIT [14, 15].

Experimentally measured atomic energy levels of Rubidium 87 are shown in Fig. 2.1. We are looking to generate EIT in this atom using it as a Λ -atom, focusing on only a few of the transitions. We will couple $5^2S_{1/2}F_2$ with $5^2P_{3/2}F_2$ using linearly polarized light for our $|2\rangle \rightarrow |3\rangle$ transition, and $5^2S_{1/2}F_1$ with $5^2P_{3/2}F_2$ using circularly polarized light for our $|1\rangle \rightarrow |3\rangle$ transition. As we intended, the $|1\rangle \rightarrow |2\rangle$ transition is dipole forbidden. These transitions in ^{87}Rb will be referred to as the $F = 2 \rightarrow F' = 2$ and $F = 1 \rightarrow F' = 2$ transitions, respectively.

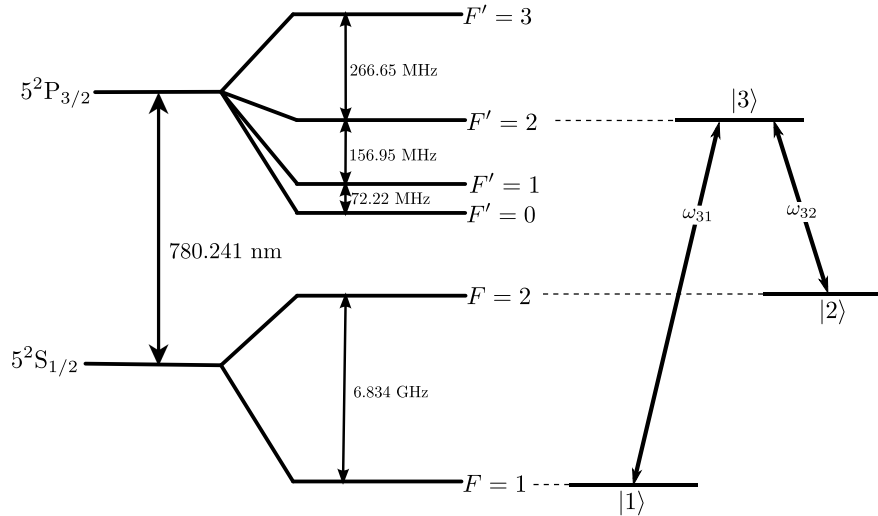


Figure 2.1: ^{87}Rb D2 lines. This figure shows the ^{87}Rb 87 D2 lines. The energy splittings are given in the units most relevant to our experiment - the energy spacings can be determined by appropriate use of physical constants (the energy difference between the ground and excited state is $\frac{hc}{(780.241\text{nm})}$, while the energy difference between the ground states is $h(6.834\text{ GHz})$). The dotted lines show the states we are using as for our Λ atom. The data for this chart was taken from Steck [16].

2.2 Optical Setup for EIT

The primary components of our experiment are the external cavity diode laser locked using saturated absorption spectroscopy onto the control laser frequency, an electro-optic modulator that generates the probe laser frequency, the rubidium cell where the EIT effects occur, and the pair of photodiodes which we use to measure the absorption.

2.2.1 Diode Laser

The diode laser is a 780 nm diode (maximum output 100 mW), set up in the Littrow configuration with an external cavity created by a piezo controlled diffraction grating for selecting the lasing mode. The laser is driven by a ILX Lightwave LDX-3525 precision current source, designed for use with laser diodes. The laser is cooled via a Peltier cooler controlled by a ILX Lightwave LDT-5910B PID Precision Thermoelectric Temperature Controller. The laser itself was partially the product of a Reed thesis [17], built with many in-house constructed components. The laser was based off a design by Arnold et al. [18].

The piezo controlled grating feedback allows the laser to be scanned across a range

of frequencies. Scanning is achieved by applying a ramp voltage from a Tektronix CFG250 function generator to a Thorlabs MDT694A piezo controller, which in turn controls a piezo crystal that shifts the laser's diffraction grating. The grating selects the wavelength that is reflected back into the diode for amplification. With piezo scanning alone, the mode hop free range of the laser diode is about 1-2 GHz. The scan range was increased to over 7 GHz by modulating the current along with the piezo crystal.

The light exiting the laser passes through an optical isolator (Conoptics Model 713A) and is then split by a 95-5 beamsplitter. The stronger beam passes on to our primary optical setup described in Section 2.2.3, while the weaker beam is fed into a Doppler free saturated absorption spectroscopy setup, described in Section 2.2.2.

2.2.2 Saturated Absorption Spectroscopy

Doppler free saturated absorption spectroscopy is a common experimental technique used to lock a laser onto the frequency of a particular hyperfine atomic transition, which we use to lock the laser onto the $F = 2 \rightarrow F' = 2$ transition of ^{87}Rb . A diagram of the spectroscopy is shown in Fig. 2.2.

Absorption spectroscopy works by scanning a probe laser in frequency across a set of atomic resonances. When the laser is at resonance, the atoms absorb the incident light. The atoms at room temperature have a Maxwell-Boltzmann distribution of velocities, which broadens the absorption peaks and obscures the hyperfine spectrum. To reveal the hyperfine structure, we apply a strong counterpropagating pump beam spatially overlapping the probe beam. The atom observes the pump and probe oppositely Doppler shifted, and so the two beams are only simultaneously at resonance with stationary atoms - at this resonance, the pump dramatically lowers the population of atoms in the ground state, reducing the absorption of the probe. This results in a dip in the absorption spectrum. A second probe beam measures the Doppler broadened spectrum, and the difference of the two probe beam intensities, as measured by a pair of photodiodes, results in peaks at hyperfine resonances free of Doppler broadening. Note that the probe beam mentioned in this section is different from the probe beam discussed throughout the rest of this thesis. For a more detailed description of this technique, check Atkinson [19].

We can scan the laser in frequency as in Section 2.2.1, and the conveniently large 7 GHz scanning range allows all four groups of D2 hyperfine lines to be visible with a single scan. A full scan is shown in Fig. 2.3 (a), and reducing the driving amplitude

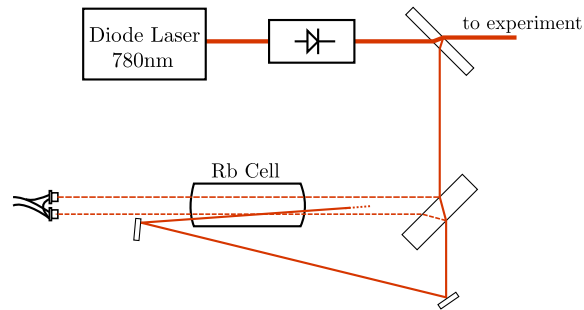


Figure 2.2: Diagram of Doppler-free saturated absorption spectroscopy. Light exiting the laser goes through an optical isolator and into a 95-5 beam splitter. The weaker beam is directed at a glass plate, off of which reflect two very weak probe beams. The stronger beam is directed to counterpropagate against one of the probe beams. One probe beam measures the Doppler broadened spectrum, while the other has resonances at hyperfine peaks. These two signals are subtracted to view the Doppler free hyperfine absorption peaks.

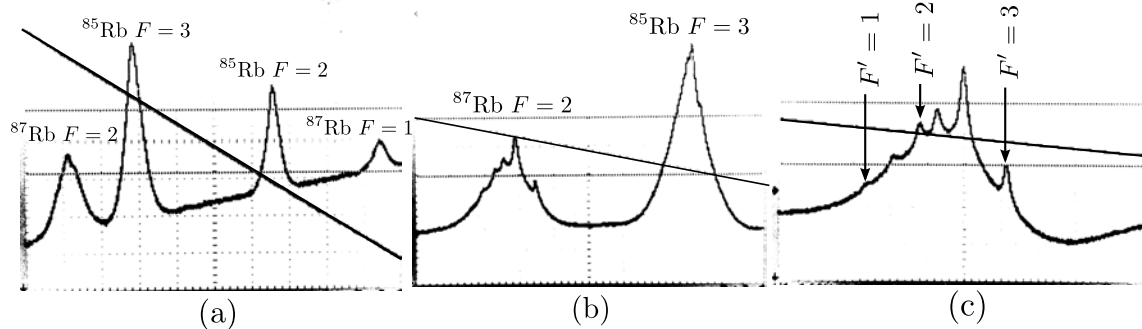


Figure 2.3: Doppler free saturated absorption spectroscopy trace. This image shows three traces using our Doppler free saturated absorption spectroscopy setup. Trace (a) is across all four sets of D2 lines, a scan of at least 7 GHz. Trace (b) is at a reduced scanning voltage showing the $^{87}\text{Rb } F = 2$ and $^{85}\text{Rb } F = 3$ transitions. Trace (c) shows the hyperfine transitions from the $F = 2$ ground state of ^{85}Rb . We lock on to the $F' = 2$ peak to generate our control laser frequency. The diagonal line across the trace is the ramp voltage - slope decreases as we reduce the scan range.

allows for distinguishing the hyperfine splitting, seen in Fig. 2.3 (b), (c). Using this spectroscopy setup, the laser is locked onto the $F = 2 \rightarrow F' = 2$ transition by observing the detector voltage of the target hyperfine peak and turning down the ramp voltage completely. The piezo voltage is manually controlled to insure that the detector voltage remains steady at the voltage level of the observed peak. Scope traces of our spectra are shown in Fig. 2.3.

2.2.3 Primary Optical Setup

Laser light locked with the saturated absorption spectroscopy setup enters our primary experimental setup shown in Fig. 2.4. It first is split by a 50-50 beamsplitting cube, where half the light is coupled into a polarization preserving optical fiber using a lens on a three axis translation mount. The laser light is linearly polarized, so a $\lambda/2$ wave plate on a rotating mount is used to orient the polarization for maximal coupling into the polarization preserving fiber. The fiber leads to an EOSpace AZ-0K5-20-PFA-PFA-780 electro-optic modulator (EOM) in a Mach Zehnder configuration. The modulator is an amplitude modulator designed to operate at wavelengths near 780 nm and has a RF and DC input. The RF input is driven by a Pulselabs Model 12050 12.5 Gb/s Pattern Generator, capable of generating clock frequencies up to 12.5 GHz at 400 mV_{p2p}. The DC input is controlled by a Dynascan 1650 Tri-output power supply. The modulator generates frequency sidebands of frequencies $\omega_{\text{input}} \pm \omega_{\text{modulation}}$, with very little leak-through of unmodulated output at frequency ω_{input} . The up-shifted sum of frequencies will be used as the probe laser, while the down-shifted difference is unwanted. The down-shifted frequency will be far off resonance with any transitions, so it can effectively be ignored¹. We describe the operation and subtleties of the EOM in Section 2.4.

Upon exiting the EOM, the modulated laser light is sent through a $\lambda/4$ wave plate, oriented to circularly polarize the laser light. The circularly polarized up-shifted laser light serves as our probe beam. It is recombined with the control beam using another 50-50 beamsplitting cube. The two beams are aligned such that they are copropagating on each of the two output paths, which is necessary for them to act on the same population of atoms. The lower path passes through a rubidium cell at room temperature containing natural rubidium (72% ⁸⁵Rb, 28% ⁸⁷Rb). It continues to a polarizing beamsplitting cube, where the horizontally polarized portion of the probe

¹This is only because we are using ⁸⁷Rb, and the peak we are locking onto for our control laser is on the outside of the D2 spectrum. The down-shifted term would not be as easily ignorable if we were using ⁸⁵Rb.

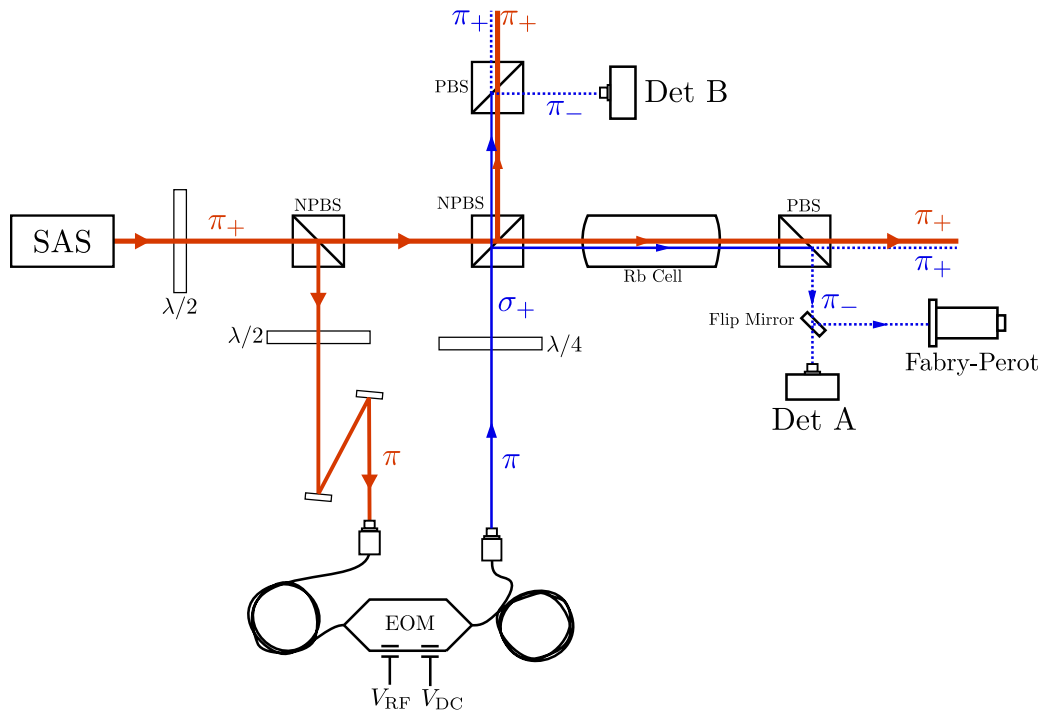


Figure 2.4: Schematic of optical setup. This is the schematic of the optical setup for measuring EIT. Linearly vertically (π_+) polarized laser light (orange) locked onto our control laser frequency enters from the saturated absorption spectroscopy setup (SAS) shown in Fig. 2.2. The light is split by a 50-50 non-polarizing beam splitting cube (NPBS). The lower path goes through a $\lambda/2$ wave plate to maximally couple into a fiber leading to an electro optic modulator (EOM). Modulated light (blue) exits from the EOM and is circularly polarized (σ_+) by a $\lambda/4$ wave plate. The probe light needs to be circularly polarized to maximally couple to the $|1\rangle \rightarrow |3\rangle$ transition. Using circularly polarized light also allows the probe laser to be recovered independently from the much stronger control laser using a polarizing beam splitting cube. Otherwise the control beam would likely saturate our detector and wash out the probe beam signal. The upper and lower beams are recombined with a NPBS and exit along two paths. The right path passes through the rubidium cell, and a polarizing beam splitting cube (PBS) splits off the horizontally polarized component of the modulated beam to be measured by a photodiode (DET A). The flip mirror can be engaged to measure the frequency splitting of the modulated beam. The vertically polarized light is blocked by a beam block. The top path follows similarly to another photodiode (DET B), except without passing through a rubidium cell. Note: The modulated and unmodulated beams are shown separated for clarity, but experimentally they must be copropagating.

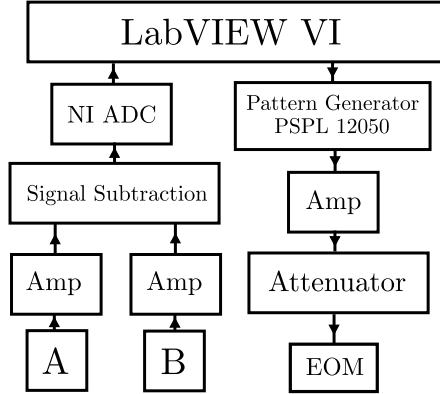


Figure 2.5: Instrument block diagram. The signals from detectors A and B are amplified by in-house amplifiers, subtracted from each other by a LT1167 differential instrument amplifier, and digitized by National Instruments USB-6009 DAQ, where a LabVIEW Virtual Instrument (VI) records the data. Meanwhile, the LabVIEW VI controls the frequency of the Pulselabs pattern generator output through a USB interface. The $400 \text{ mV}_{\text{p2p}}$ output is amplified to $\sim 8 \text{ V}_{\text{p2p}}$ and attenuated to $\sim 800\text{-}1000 \text{ mV}_{\text{p2p}}$ to drive the EOM.

beam is split from the combined beam and is aligned onto a photodiode detector. The remaining vertically polarized beam is unneeded and is absorbed by a beam block. The other path is the same in all respects, except that it does not have a rubidium cell. This is used as a ‘background’ subtraction, which helps filter out spurious sources of noise.

2.3 Electronics

We now move to describe the electronics behind our setup. A block diagram is shown in Fig. 2.5. The Pulselabs pattern generator was designed for use in the data communication industry primarily to generate streams of bits, and as such, it does not have a frequency ramping feature. However, it does have a USB interface that can be controlled through National Instrument’s LabVIEW in a similar fashion to a GPIB interface. This allowed us to design a program to step through modulation frequencies and measure the intensity of the probe laser at each modulation frequency. The scan rate was limited by the pattern generator’s delay in changing output frequencies (on the order of 2-3 seconds), which unfortunately made real-time scans impossible. The pattern generator output ($400 \text{ mV}_{\text{p2p}}$) was also too weak to properly drive the EOM (we found that a EOM RF voltage of $\sim 1 \text{ V}_{\text{p2p}}$ was sufficient), so the signal was amplified by a JDS Uniphase Optical Modulator Driver Model H301-2310 by a

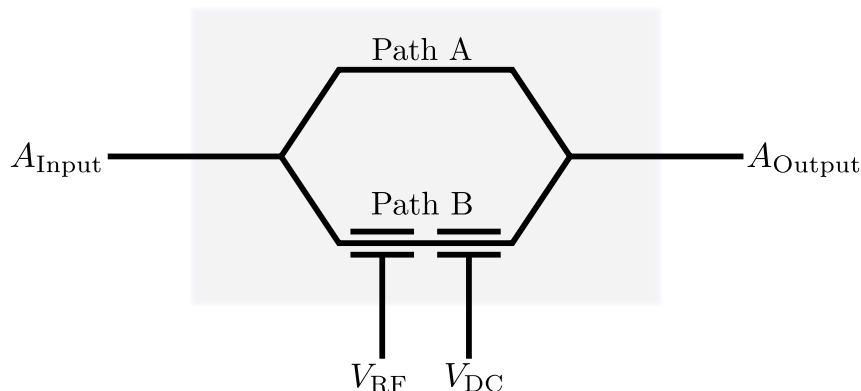


Figure 2.6: Schematic of an electro-optic modulator. Input light is split to travel down two paths in a material (Lithium Niobate) that has an index of refraction that is highly sensitive to electric fields. Path A has a fixed optical length, while Path B has an optical length that varies based on the applied electric field. A phase shift develops between the light on each path, such that when the paths merge interference occurs. The amount of interference is controlled by the applied field.

factor of 20, and then attenuated by a series of three signal splitters capped with 50Ω resistors (a factor of 8 attenuation). The attenuated output was measured to be ~ 1 V_{p2p} at 5GHz, with a drop to ~ 800 mV_{p2p} at 8 GHz. All RF outputs and measurements have a nominal impedance of 50Ω .

During a scan, each photodiode measures the incident probe light, and the signal is amplified by an in-house built amplifier. The amplified photodiode outputs are on the order of 0-10 V and are fed into a LT1167 differential instrument amplifier. The input signals to the LT1167 are attenuated with 10-turn 1 $k\Omega$ potentiometers to match the amplitudes. The signals are then subtracted and amplified, ideally leaving a signal due solely to the absorption of the probe as it passed through the rubidium. The output of the LT1157 is digitized by a USB-6009 DAQ, and plotted against the modulation frequency using LabVIEW.

2.4 Electro-Optic Modulator

An amplitude electro-optic modulator (EOM) operates by splitting an input beam into two paths - one path travels through a material that has an optical path length that varies with an applied electric field. When the two beams recombine, they are out of phase by an amount that is a function of the applied voltage. This results in interference that is directly controlled by an external voltage, which can be tuned to result in destructive or constructive interference. This is shown schematically in

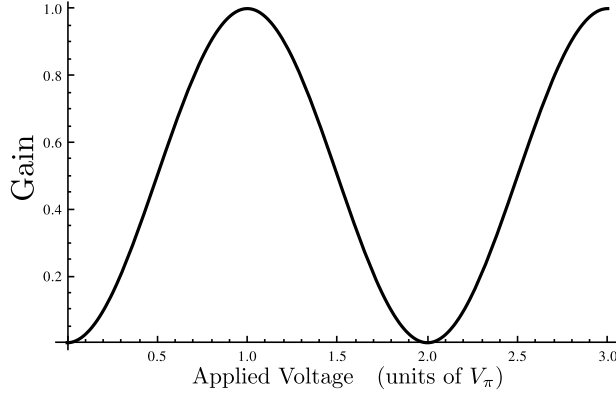


Figure 2.7: Gain curve of an amplitude EOM.

Fig. 2.6.

The operation of an EOM can be described by a relation between the input and output amplitudes, $I_{\text{output}} = I_{\text{input}}G(V(t))$. $G(t)$ is a gain curve given by

$$G(t) = \sin^2 \left(V(t) \frac{\pi}{2V_\pi} + \frac{\phi}{2} \right) = \frac{1}{2} - \frac{1}{2} \cos \left(V(t) \frac{\pi}{V_\pi} + \phi \right), \quad (2.1)$$

where V_π is the voltage necessary to cause a phase shift of π , and ϕ is the phase difference in absence of any fields - both are intrinsic properties of a particular modulator. It is common for V_π to have frequency dependence, but our EOM has $V_\pi = 1.2\text{V}$ for both DC and RF signals. The gain curve is plotted in Fig. 2.7.

We will drive our EOM with a sinusoidal voltage with a DC offset, so we set $V(t) = V_{\text{DC}} + V_{\text{RF}} \sin(\omega_{\text{RF}}t)$, where ω_{RF} is our modulation frequency. We also can choose a particular V_{DC} to cancel out the arbitrary phase ϕ , so we may as well set $\phi = 0$:

$$G(t) = \frac{1}{2} - \frac{1}{2} \cos \left(V_{\text{DC}} + V_{\text{RF}} \frac{\pi}{V_\pi} \sin(\omega_{\text{RF}}t) \right). \quad (2.2)$$

We can expand this using a trigonometric identity:

$$G(t) = \frac{1}{2} \left(1 - \cos \left(\frac{V_{\text{DC}}\pi}{V_\pi} \right) \cos \left(\frac{V_{\text{RF}}\pi}{V_\pi} \sin(\omega_{\text{RF}}t) \right) + \sin \left(\frac{V_{\text{DC}}\pi}{V_\pi} \right) \sin \left(\frac{V_{\text{RF}}\pi}{V_\pi} \sin(\omega_{\text{RF}}t) \right) \right). \quad (2.3)$$

There is a useful set of identities relating a composition of trigonometric functions to a sum of Bessel functions known as the Jacobi-Anger expansion - we will use the

following two:

$$\sin(z \sin \theta) = 2 \sum_{n=1}^{\infty} J_{2n-1}(z) \sin((2n-1)\theta), \quad (2.4)$$

$$\cos(z \sin \theta) = J_0(z) + 2 \sum_{n=1}^{\infty} J_{2n}(z) \cos(2n\theta). \quad (2.5)$$

J_n is the n^{th} Bessel function of the first kind. Applying this expansion to Eq. (2.3) we have:

$$G(t) = \frac{1}{2} \left(1 - \cos \left(\frac{V_{\text{DC}}\pi}{V_\pi} \right) \left[J_0 \left(\frac{V_{\text{RF}}\pi}{V_\pi} \right) + 2 \sum_{n=1}^{\infty} J_{2n} \left(\frac{V_{\text{RF}}\pi}{V_\pi} \right) \cos(2n\omega_{\text{RF}}t) \right] \right. \\ \left. + 2 \sin \left(\frac{V_{\text{DC}}\pi}{V_\pi} \right) \sum_{n=1}^{\infty} J_{2n-1} \left(\frac{V_{\text{RF}}\pi}{V_\pi} \right) \sin((2n-1)\omega_{\text{RF}}t) \right). \quad (2.6)$$

We want to maximize the amplitude of the term containing $\sin(\omega_{\text{RF}}t)$, as it will lead to sidebands of frequency $\omega_p \pm \omega_{\text{RF}}$. We also will want to minimize the constant term $\frac{1}{2} \left(1 - \cos \left(\frac{V_{\text{DC}}\pi}{V_\pi} \right) J_0 \left(\frac{V_{\text{RF}}\pi}{V_\pi} \right) \right)$, for this will correspond to leakage of our control frequency into our probe beam. Thus, let us maximize the difference of these amplitudes:

$$\text{Maximize: } \underbrace{J_1 \left(\frac{V_{\text{RF}}\pi}{V_\pi} \right) \left| \sin \left(\frac{V_{\text{DC}}\pi}{V_\pi} \right) \right|}_{\text{amplitude of } \sin(\omega_{\text{RF}}t)} - \underbrace{\frac{1}{2} \left(1 - \cos \left(\frac{V_{\text{DC}}\pi}{V_\pi} \right) J_0 \left(\frac{V_{\text{RF}}\pi}{V_\pi} \right) \right)}_{\text{amplitude of constant term}} \quad (2.7)$$

Numerically maximizing this function for the parameters V_{DC} and V_{RF} we find a number of solutions, each with approximately the same ratio of spectral power. One such solution is $V_{\text{RF}} \approx 0.492V_\pi$, $V_{\text{DC}} \approx 0.370V_\pi$. This corresponds to a gain of:

$$G(t) = 0.404 + 0.518 \sin(\omega_{\text{RF}}t) + [\text{higher frequency terms}]. \quad (2.8)$$

Dropping higher terms and applying this to an input laser of with electric field magnitude $E_{\text{in}}(t) = E_0 \sin(\omega_c t)$ gives:

$$E_{\text{out}} = G(t)E_{\text{in}}(t) \approx E_0 (0.404 + 0.518 \sin(\omega_{\text{RF}}t)) \sin(\omega_c t). \quad (2.9)$$

Expanding this with a trigonometric identity gives:

$$E_{\text{out}} \approx E_0 [(0.404) \sin \omega_c t + (0.259) \sin(\omega_c - \omega_{\text{RF}}t) - (0.259) \sin(\omega_c + \omega_{\text{RF}}t)]. \quad (2.10)$$

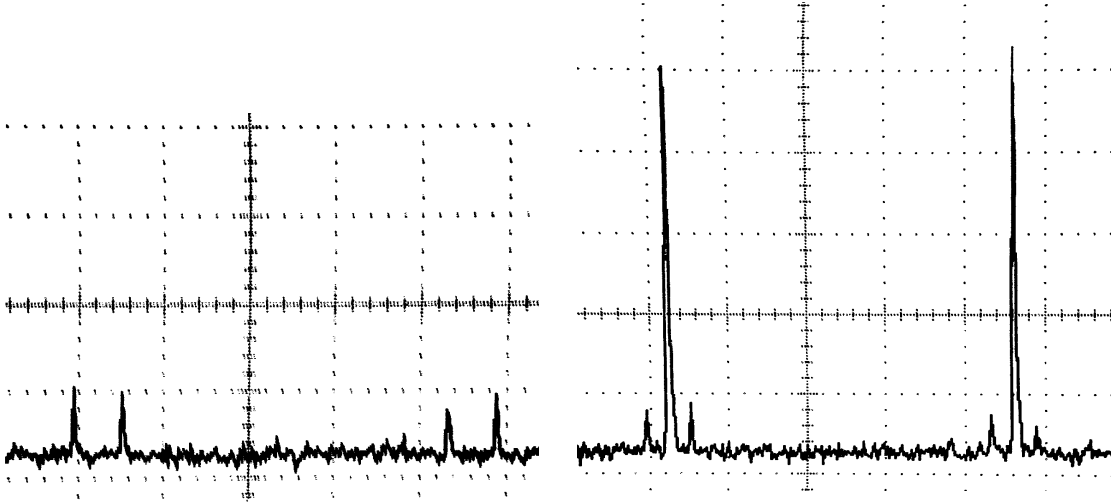


Figure 2.8: EOM viewed on Fabry-Perot interferometer, DC adjustment. This figure shows the EOM spectral output with a modulation of 1.4 GHz as measured with a Fabry-Perot interferometer. (a) and (b) differ only by the DC offset which has the outcome of nearly eliminating all input frequency in the EOM output. The free spectral range of the Fabry-Perot interferometer is given as 1.5 GHz (the spacing between the large peaks), and the side peaks are spaced only slightly less than this, indicating that our modulation is properly generating sidebands.

Our end result is that the output will still contain a substantial amount of the control frequency even when tuned optimally. Interestingly, this does not match what we find in our physical EOM.

The output of the EOM was viewed with a scanning Fabry-Perot interferometer (Thorlabs SA200-6A with free spectral range of 1.5 GHz) allowing us to insure we were generating sidebands with the EOM for modulation frequencies lower than 1.5 GHz. Additionally, we discovered that we could adjust the DC offset such that the output contained almost none of the input frequency, and only contained two significant sidebands. These effects are shown in Fig. 2.8, where the DC offset is tuned to remove all input frequency from the output.

More predicted is the ability to generate a number of sidebands of higher frequency multiples, as we saw using the Jacobi-Anger Expansion in Eq. (2.6). We show this measured result in Fig. 2.9. These sidebands could potentially be used to scan beyond the 12.5 GHz limit of our pattern generator by employing these higher frequency multiples.

The surprising ability to reduce the output to only a pair of sidebands is quite beneficial for our experiment, as it means we can remove all light at the control laser frequency by blocking the non-modulated path, and that our probe beam will have

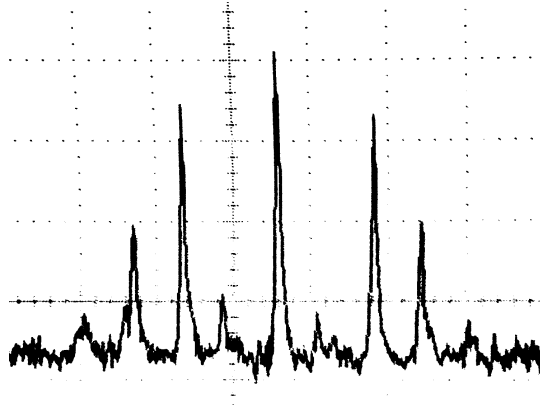


Figure 2.9: EOM viewed on Fabry-Perot interferometer, large V_{RF} . This figure shows the EOM spectral output measured with a Fabry-Perot interferometer with a sufficiently high EOM modulation voltage to generate higher frequency orders.

a high signal-to-noise ratio. Possible reasons for this windfall are that the gain curve may not be as sinusoidal as we assumed in Eq. (2.1). Measuring the gain curve shape could be done by monitoring the intensity of the output as a function of the input, but this has not been performed.

2.5 Data Collection

In this section we describe the procedure used for collecting the absorption spectra shown in Chapter 3.

First, the laser current is increased until the approximate desired power level is reached (lasing starts at ~ 33 mA, see Fig. 2.10). The spectroscopy setup is then used to locate absorption spectra of the ^{87}Rb $F = 2$ lines by adjusting the piezo controller and laser current. Once found, the piezo ramping is turned down while keeping the $F' = 2$ centered using the piezo DC offset adjustment. DC coupling should be enabled on the oscilloscope so that the cursor function can be used to mark the height of the $F' = 2$ peak. This mark will be used to insure that when the peak drifts, it can be found again without turning on the ramp signal.

Next, the Fabry-Perot interferometer is engaged to view the spectral output of our laser by flipping up the flip mirror noted in Fig. 2.4. The DC power supply for the EOM is engaged, and adjusted so that a strong central peak is visible from the interferometer. We view this to insure that our laser is operating on only one mode - this is done since if side peaks are visible, the laser is more likely to mode hop, ruining any scans in progress. The mode peaks also reduce visibility of our modulated

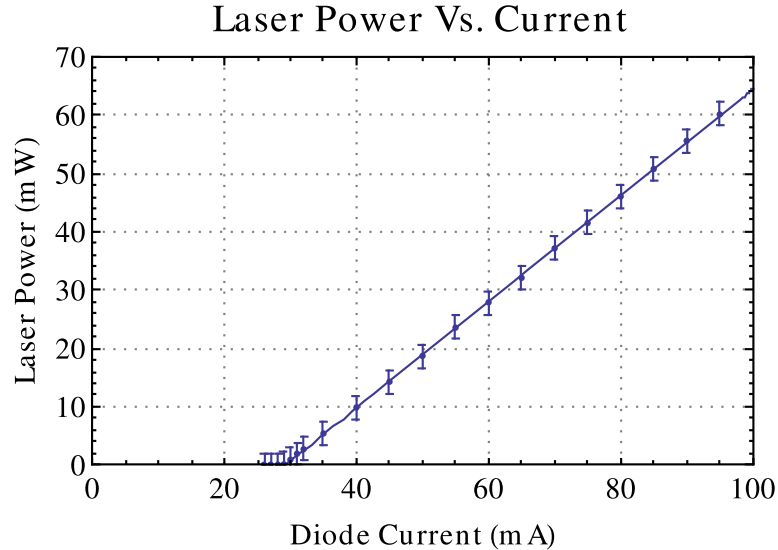


Figure 2.10: Laser Power vs. Current. A plot of the laser power measured immediately out of the enclosure as a function of the current applied to the diode.

side peaks and power fluctuations are more evident. If competing laser modes are observed, the current and piezo are shifted slightly to reduce them.

The power is next engaged to the JDSU Optical Modulator Driver, and then to the Pulselabs pattern generator².

For testing and calibration purposes a Agilent E4411B Spectrum Analyzer is used instead of the Pulselabs pattern generator to generate a frequency ramp from 0 to 1.5 GHz (using the on-board tracking generator). This is particularly useful since it allows for real-time scanning, and adjustments of gain. For performing this calibration, we locked onto the $^{87}\text{Rb}F = 2$ peaks, and modulated our beam to observe the $^{85}\text{Rb}F = 3$ peaks. At this point, the attenuation and gain on the LT1167 were adjusted to maximize the signal.

Once our measurement system is optimized, we return to using the Pulselab pattern generator for modulations around 6.8 GHz, the splitting between the ground levels of ^{87}Rb . The modulation frequency is set to around 7 GHz³, and the EOM output is observed on the Fabry-Perot interferometer. While this is operating beyond the free spectral range of our interferometer, we are using this only to confirm that there

²RF devices are highly sensitive, especially amplifiers - before power is engaged to the amplifier, all nodes should be terminated at an impedance matched device or resistor. Additionally, no RF signals should be active before the amplifier is turned on. This is particularly important for the Pulselab pattern generator - the clock output is continually active whenever the device has power, so it should be turned on last.

³The precise value is not important, only that it should be in the range of the intended modulation scan, and not a multiple of 1.5 GHz, for this would hide the sidebands.

are sidebands and to determine their relative power compared to the control laser frequency. The DC offset on the modulator is now adjusted to minimize the coupling laser light - usually it can be set such that it is not visible above the background noise of the detector.

At this point the measurements are taken of the power of both the probe beam and the control beam immediately before they enter the rubidium chamber (using a Newport 9180-IR-003 Detector with a Newport 1917-R Optical Power Meter). The control beam is blocked with a beam block for the probe beam measurement and vice versa. Note that the probe beam power measured in this setup is twice the power of the probe power recorded, since the difference sideband contributes equally to the power but is not part of our signal for measuring EIT.

The setup is now ready for scanning - the scan range and step size are set in LabVIEW, and the flip mirror is disengaged. Results of this process are shown in Chapter 3.

Chapter 3

Results and Discussion

In this chapter we discuss the EIT characteristics we measured in thermal rubidium atoms using the setup in the previous chapter. We will also discuss why the results we do see are not as sharply defined as those predicted in Chapter 1 Section 1.9.

3.1 Collected Data

The plots of the measured probe beam absorption as a function of modulation frequency are shown in Fig. 3.1. All scans are performed over the $F = 1 \rightarrow F' = 2$ peak with the modulation frequency centered at 6.8 GHz. Fig. 3.1 shows scans at two power levels: the run shown in panel (a) was carried out with a control beam power of 1.15 mW and a probe beam power of 42.5 μ W, the run shown in panel (b) was carried out with a control beam power of 4 mW and a probe beam power of 75 μ W. For each power level, two sets of scans were performed. One set of scans was from a modulation frequency range of 5.8GHz to 7.4GHz with a step size of 80MHz, capturing most the Doppler broadened peak. The other set of scans is over a range extending from 6.5 GHz to 7.0 GHz with a step size of 20 MHz, providing higher resolution at the resonance. Each plot depicts the average of 6 scans, with the error bars showing the standard deviation.

3.1.1 Corrections

To generate these plots, some manual correction to our data was necessary. Electro-optic modulators tend to have shifts in their gain curve over time. While the V_π voltage tends to be steady, the DC voltage offset that corresponds to a particular output amplitude changes - in other words, the ϕ defined Eq. (2.1) has some weak

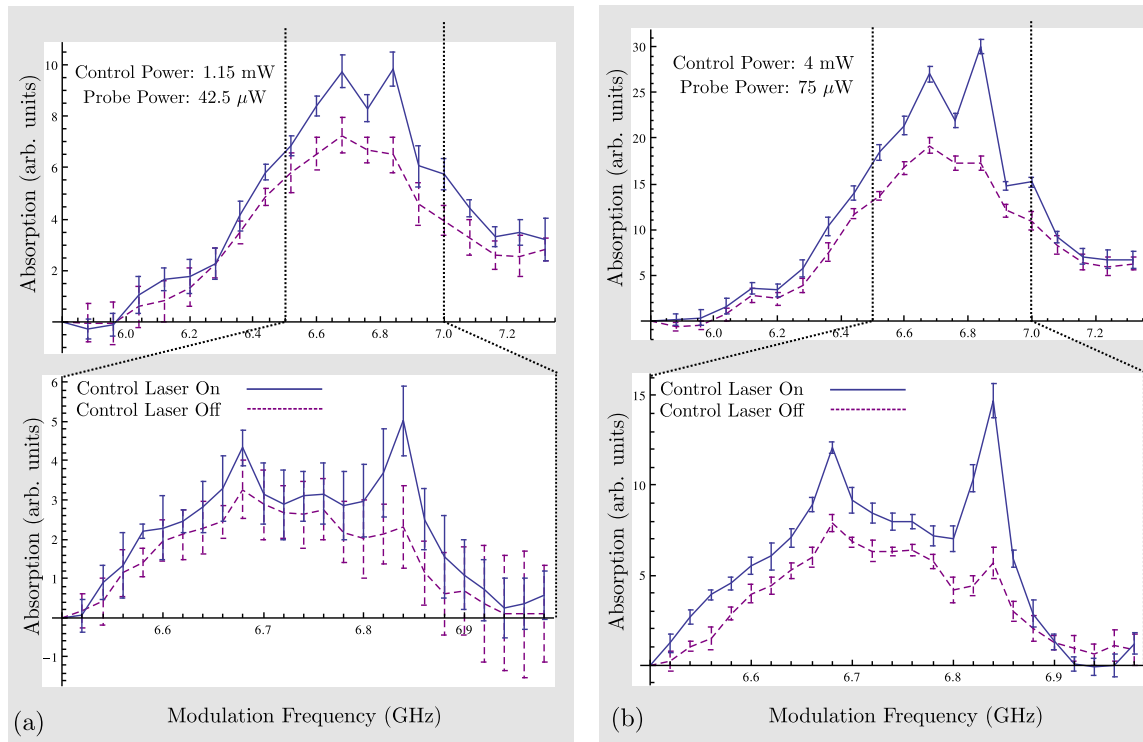


Figure 3.1: Experimental EIT absorption spectra. Plots of absorption spectrum of ^{87}Rb as a function of the modulation frequency at two different control beam powers. Panel (a) is with a control beam power of 1.15 mW, panel (b) is with a control beam power of 4 mW. The resonance is anticipated to be at 6.8 GHz modulation. Each data point is the average over 6 scans, with the error bars showing the standard deviation.

time dependence. The effect is to allow more and more light at the control frequency to leak into the probe beam over time. While the intensity of the control beam leakage is too low to significantly change the medium's properties (which we discuss later), it is still circularly polarized light, part of which will be redirected onto the photodiodes causing an offset, an offset that changes as the EOM drifts. This causes a slow drift between subsequent data runs, so that absolute intensities cannot be compared. To allow comparison between data sets, we translate all absorption curves so they begin at 0. This accounts for the offset between subsequent runs. It does not account for the drift over a single run. The magnitude of the drift is about 0.5 V over a single run and appears to be a linear drift. Our plots have not been corrected for the single run drift.

3.1.2 Analysis

The first observation from the plots shown in Fig. 3.1 is that applying the control laser produces a significant dip near the frequency at which the absorption is maximum when the control laser is inactive. This is precisely the effect we are expecting to see for a system demonstrating EIT. Our dip, however, is very shallow. The shallowness of the dip is not unexpected for several reasons. As we saw in Fig. 1.5, a decrease in coherence lifetime reduces the depth of EIT peaks. In our system the coherence lifetime is in part a function of how long atoms stay in the fields. Since the atoms are moving, they will drift in and out of the path of the laser. Each time a new atom enters or an excited atom leaves the beam path, we effectively have a decay. Thus, the lifetime of the excited states decreases (an increase in γ_{13} and γ_{12}). Additionally, low coupling power results in a reduction in the visibility of EIT as seen in Fig. 1.4. Our measured coupling power is lower than those used in other experimental setups. For example in the observation of EIT by Olson and Mayer [15], somewhat shallow EIT features are observed with a control laser of 12 mW, a power three times greater than our highest power run at 4 mW. Furthermore, unless the probe and control beams are perfectly aligned, we expect to observe the EIT features to be superimposed on the top of a typical Doppler broadened Gaussian peak. As is illustrated in Fig. 3.2, this is due to an effect where some atoms in the path of the probe beam are not being irradiated by the control beam. Therefore, unless we maintain high coherence, have a sufficiently strong control laser, and ideal alignment, our dip is not expected to drop down to zero.

Another observation is that when the control laser is engaged, the overall ab-

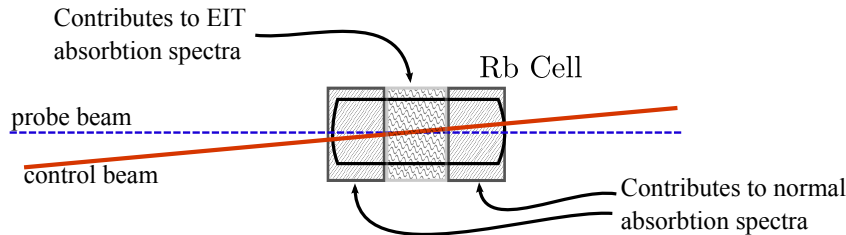


Figure 3.2: Spatial dependence of absorption contributions. This figure shows that when the control beam and probe beam are not entirely copropagating, we gain contributions to the absorption spectra from both atoms exhibiting EIT and normal Rb that is not strongly coupled to the control beam. This figure exaggerates the angles between the beams.

sorption appears to increase. Initially, one may presume this is the opposite of the anticipated effect, as EIT is intended to create a transparency at resonance. However, this can be cleanly attributed to hyperfine pumping of the atoms into the ground state, depicted in Fig. 3.3. When the control beam is inactive, the population of the system will not all be in the state $|1\rangle$. Rather, a substantial portion will be in the $|2\rangle$ state as well¹. When we apply the control laser, any atoms in the $|2\rangle$ state will oscillate between states $|2\rangle$ and $|3\rangle$ until a spontaneous decay sends it from $|3\rangle$ down to $|1\rangle$. This process repeats until the population is almost entirely in the state $|1\rangle$. Since we have more atoms available in the ground state, we expect to see a stronger absorption in general when the control laser is active.

There is one particularly curious aspect of the plots in Fig. 3.1. When the control laser is blocked, we notice distinct spiked features in the spectrum. This is unusual, as we would expect to see a featureless Doppler broadened peak. The features also line up with features we have presumed to be due to EIT. A possible explanation for this is leakage of control laser light into the probe beam through the EOM when the control beam is blocked. This may result in dampened EIT features being visible even when the primary source of control laser light is blocked. However, as the probe beam is less than a 20th the power of the control beam, and we have observed that the quantity of control laser light in the probe beam can be minimized dramatically, this seems unlikely. Taking a spectrum while the control beam is locked far from any resonances would be a method to confirm this. If the features are still visible, they are the result of some process other than EIT, and their alignment with our supposed EIT

¹If the atoms were brought to colder temperatures, and left to decay for a sufficiently long time, would the atoms end up primarily in the $|1\rangle$ state. However, the atoms are at room temperature, and thermal excitations are sufficient to populate $|2\rangle$. We can see proof of this when we perform saturated absorption spectroscopy. The absorption peaks for the $|2\rangle$ transitions are actually *stronger* than for the $|1\rangle$ transitions, indicating a greater population in the $|2\rangle$ state than in the $|1\rangle$ state.

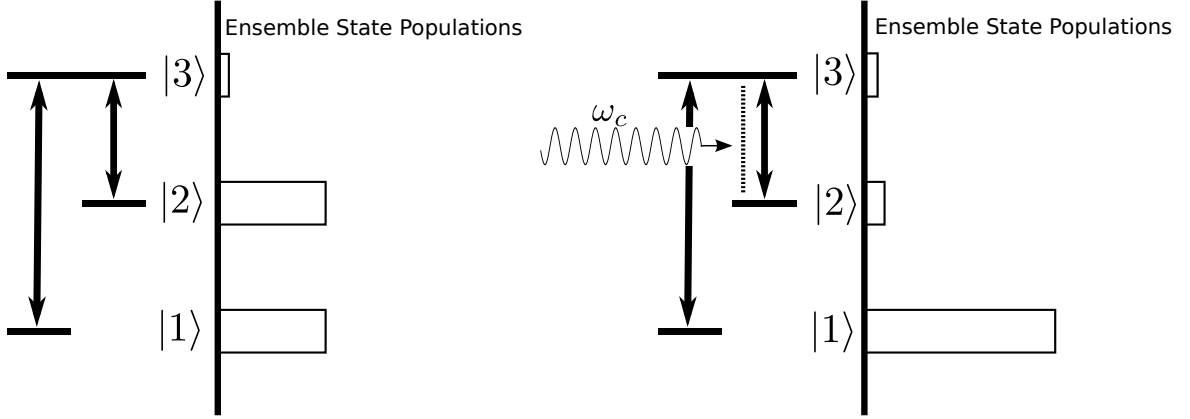


Figure 3.3: Pumping effects. This figure demonstrates the effect of hyperfine pumping. At room temperature, a substantial amount of atoms are both states $|1\rangle$ and $|2\rangle$. When we apply the control laser, any atoms in the $|2\rangle$ state will oscillate between states $|2\rangle$ and $|3\rangle$ until a spontaneous decay sends it from $|3\rangle$ down to $|1\rangle$. This process repeats until the population is almost entirely in the state $|1\rangle$. On the left we depict the relative populations before and after the hyperfine pumping.

features makes our observation of EIT slightly suspect. This measurement was not performed due to time constraints. While this casts some shadow on our observation of EIT, the dip at resonance is a distinctive feature that is very likely the result of EIT and not the result of another process².

We conclude that our results tentatively indicate we have some level of EIT occurring, though for absolute confidence, and to actually probe other interesting aspects of EIT, the absorption dip needs to be greatly strengthened. We look at possibilities for increasing the EIT response in the next section.

3.2 Improvements

In this section we overview possible improvements to our experimental setup and methods.

3.2.1 Reducing Decoherence

We noted that our experimental setup generated a relatively small absorption dip, compared to other similar similar experiments, with contributing factors being a large

²Initially the possibility was considered that we might be observing a saturation effect. This is not the case, because the control laser is operating on an entirely different population of atoms than the probe laser, so it cannot be saturating the transition. Saturation is a possibility in V and cascade systems, but it is not in Λ systems [20].

γ_{12} , a weaker control laser, and non-idealized alignment. We address possible solutions to all of these:

Let us first look at reducing the decoherence term γ_{12} . This can be lowered by a number of methods. We saw in the previous section that the rate of atoms entering and leaving the beam contribute to this term. We want to maximize the number of atoms in the beam, while minimizing the number of atoms that can enter and leave the beam - this amounts to maximizing the volume while minimizing the surface area. Increasing the beam width of the combined lasers before they pass through the rubidium with a pair of lenses would accomplish this. This has the additional benefit of increasing the alignment of our copropagating beams, for wider beams can be more accurately aligned. Another method to lower γ_{12} is to apply an inert buffer gas. This reduces the number of atom-atom interactions, another contribution to γ_{12} . However, while this is a viable option, it would be more difficult to implement than additional lenses.

Next, the power of our laser was not near the maximum when we performed this experiment. This was a choice that was primarily due to issues we had with detector saturation. The saturation was a result of the amount of control beam leakage through the upper polarizing beam splitting cube (see Fig. 2.4). The amount of leaked control beam light that is sent to Det B is far larger than the amount of control beam light sent to Det A. The difference in signal causes a huge DC shift when the control laser is blocked or revealed. We accounted for this difference in signal by lowering the gain on Det B's amplifier. However, this reduces the effectiveness of our subtraction arm, as the probe amplitudes need to be weighted similarly for useful subtraction. This issue could be fixed simply by purchasing a new polarizing beamsplitting cube.

3.2.2 EOM Drift

One difficulty with our experimental setup is the EOM drift over time. The effect is likely due in part to temperature change. This effect could be mitigated by implementing a Peltier PID temperature control system similar to those on the laser controllers. This would increase the consistency of our measurements, and allow for a more simplified data collection procedure.

3.2.3 Real Time Scanning

Real-time scanning of a spectrum demonstrating EIT was an initial goal of our experimental setup, as it would provide a method for easily optimizing our setup, and

provide higher resolution scans. This was not realized, as the Picosecond pattern generator is not capable of rapidly changing frequencies. It is feasible to achieve this in a future setup using an RF mixer to mix the output of the pattern generator and the Agilent E4411B Spectrum Analyzer 1.5 GHz tracking generator. An RF mixer works in a similar fashion to the electro-optic modulator, generating output frequencies of both a sum and difference of the input frequencies. Mixing the Pulselabs pattern generator output of ~ 6 GHz with the Spectrum Analyzer frequency ramp from 0 to 1.5 GHz would generate a frequency ramp from 6 GHz to 7.5 GHz. This would nicely scan across the 6.8 GHz ground state splitting. Applying this voltage to the EOM would generate a nice probe frequency ramp. An RF mixer with the appropriate frequency range is already available in the lab. To get the ramp working, however, it is likely that a bandpass filter would need to be purchased to filter out the 6 GHz signal, and the difference signal.

Conclusion

*Life is filigree work. What is written clearly is not worth much,
it's the transparency that counts.*

-Louis Ferdinand Céline

In this thesis we set out to observe electromagnetically induced transparency in thermal rubidium vapor. We first derived the electric susceptibility of a three level atom and demonstrated that the optical properties of the medium are highly modified when a control laser is coupled to our system. We further showed that these properties should still be evident even when our medium is inhomogeneously Doppler broadened. Our experimental section began by showing that Rubidium 87 is a viable candidate for use as a three level Λ atom, and we proposed a single laser experimental setup designed to measure the absorption spectrum using a probe beam, while simultaneously coupling the system with a control beam. This thesis culminates with an observation of a distinct dip in the absorption spectrum when the control beam was applied to our medium, which we have attributed to EIT.

References

- [1] S. E. Harris, J. E. Field, and A. Imamoglu, “Nonlinear Optical Processes Using Electromagnetically Induced Transparency,” *Phys. Rev. Lett.* **64**, 1107–1110 (1990).
- [2] K. J. Boller, A. Imamoglu, and S. E. Harris, “Observation of Electromagnetically Induced Transparency,” *Phys. Rev. Lett.* **66**, 2593–2596 (1991).
- [3] J. E. Field, K. H. Hahn, and S. E. Harris, “Observation of Electromagnetically Induced Transparency in Collisionally Broadened Lead Vapor,” *Phys. Rev. Lett.* **67**, 3062–3065 (1991).
- [4] M. Jain, H. Xia, G. Y. Yin, A. J. Merriam, and S. E. Harris, “Efficient Nonlinear Frequency Conversion with Maximal Atomic Coherence,” *Phys. Rev. Lett.* **77**, 4326–4329 (1996).
- [5] D. Budker, D. F. Kimball, S. M. Rochester, and V. V. Yashchuk, “Nonlinear Magneto-optics and Reduced Group Velocity of Light in Atomic Vapor with Slow Ground State Relaxation,” *Phys. Rev. Lett.* **83**, 1767–1770 (1999).
- [6] H. Y. Ling, Y. Q. Li, and M. Xiao, “Electromagnetically induced grating: Homogeneously broadened medium,” *Phys. Rev. A* **57**, 1338–1344 (1998).
- [7] M. Fleischhauer, A. Imamoglu, and J. P. Marangos, “Electromagnetically induced transparency: Optics in coherent media,” *Revs. Mod. Phys.* **77**, 633–673 (2005).
- [8] J. P. Marangos, “Topical review electromagnetically induced transparency,” *J. Modern Optics* **45**, 471–503 (1998).
- [9] S. E. Harris, “Electromagnetically induced transparency,” *Physics Today* **50(7)**, 36–42 (1997).

-
- [10] R. Bennink, Ph.D. thesis, University of Rochester (2004).
- [11] M. Fleischhauer and M. D. Lukin, “Dark-State Polaritons in Electromagnetically Induced Transparency,” *Phys. Rev. Lett.* **84**, 5094–5097 (2000).
- [12] J. O. Weatherall, Ph.D. thesis, Stevens Institute of Technology (2009).
- [13] M. O. Scully and M. S. Zubairy, *Quantum optics* (Cambridge University Press, 2006).
- [14] M. Yan, E. G. Rickey, and Y. F. Zhu, “Electromagnetically Induced Transparency in Cold Rubidium Atoms,” *J. Opt. Soc. Am. B* **18**, 1057–1062 (2001).
- [15] A. J. Olson and S. K. Mayer, “Electromagnetically induced transparency in rubidium,” *Am. J. Phys.* **77**, 116–121 (2009).
- [16] D. A. Steck, “Rubidium 87 D Line Data,” (2010), (revision 2.1.3, 23 December 2010), Available online at: <http://steck.us/alkalidata>.
- [17] A. C. Lily, Undergraduate thesis, Reed College (2004).
- [18] A. S. Arnold, J. S. Wilson, and M. G. Boshier, “A simple extended-cavity diode laser,” *Rev. Sci. Instrum.* **69**, 1236–1239 (1998).
- [19] F. G. Atkinson, Undergraduate thesis, Reed College (1996).
- [20] A. Lazoudis, T. Kirova, E. H. Ahmed, P. Qi, J. Huennekens, and A. M. Lyyra, “Electromagnetically induced transparency in an open V-type molecular system,” *Phys. Rev. A* **83**, 063419 (2011).